Boundary-Layer Meteorology (2023) 188:285–320
https://doi.org/10.1007/s10546-023-00814-0

RESEARCH ARTICLE

Statistics of Wind Farm Wakes for Different Layouts and Ground Roughness

Zewei Wang[1,2] · Guodan Dong[1,2] · Zhaobin Li[1,2] · Xiaolei Yang[1,2]

Received: 25 January 2023 / Accepted: 4 May 2023 / Published online: 2 June 2023

Abstract
In this work, wakes of wind farms are investigated using large-eddy simulation with an actuator disk model for the wind turbine. The effects of streamwise turbine spacings, number of wind turbine rows and roughness lengths of ground surface on the characteristics of wind farm wakes are examined. The simulation results showed that the effects of S_x (streamwise turbine spacings) are mainly located in the near wake of wind farm (less than 20 rotor diameters downstream from the last row of the wind farm), where the turbulence intensity is higher for smaller values of S_x. In the far wake of wind farms (more than 90 rotor diameters downstream from the last row of the wind farm), the streamwise velocity deficit as well as the Reynolds stresses from cases with different streamwise turbine spacings are close to each other. For cases with more wind turbine rows (N_{row}) and larger roughness length of ground surface (k_0), faster velocity recovery and higher turbulence intensity are observed. Terms in the budget equation for mean kinetic energy (MKE) are examined. The analyses showed that the vertical MKE transport via mean convection and turbulence convection plays a dominant role in the velocity recovery in wind farm wakes, being different from the wind farm region where streamwise MKE flux due to mean convection also plays a role. Lastly, an analytical model for the velocity deficit in wind farm wake is proposed based on the Emeis model. Improvements on the model predictions are observed for all the simulated cases. The velocity deficit at one downstream location of the wind farm needs to be given is one major limitation of the analytical model of this type.

Keywords Wind farm · Wakes · Boundary layer

1 Introduction

In wind energy, electricity is generated from the kinetic energy of the atmospheric boundary layer flow via wind farms often consisting of many wind turbines. With the rapid development

✉ Xiaolei Yang
xyang@imech.ac.cn

1 The State Key Laboratory of Nonlinear Mechanics, Institute of Mechanics, Chinese Academy of Sciences, Beijing, China

2 School of Engineering Sciences, University of Chinese Academy of Sciences, Beijing, China

of wind energy in many countries, the farm-scale wake interaction needs to be accounted for in both the design (e.g., the siting of downstream wind farms) and operation (e.g., the optimal operation of several wind farms) stages of a wind energy project.

The wake of a wind farm, which is featured by velocity losses and high levels of turbulence intensity, negatively impacts the performance of downstream wind farms (Christiansen and Hasager 2005; Hasager et al. 2015; Lundquist et al. 2019; Syed et al. 2022; Stieren and Stevens 2022). Because of the complexity of the interaction between wind farm wakes and atmospheric flows, and the complexity of the operational conditions with many factors involved (e.g., the wind farm layout, the installed capacity and the stability of the atmospheric boundary layer), the physics of wind farm wakes is yet to be fully understood.

Field observations have shown that the wake of a wind farm can persist for a very long distance. Christiansen and Hasager (2005) identified wake effects near two large offshore wind farms, i.e., Horns Rev and Nysted, from satellite SAR (Synthetic Aperture Radar) data, and observed that the velocity deficit reduces to 2% of the free stream velocity at ~ 5 km and ~ 20 km downstream of the wind farm for unstable and near-neutral atmospheric conditions, respectively. The aircraft measurements on the wake of the offshore wind farms in German Bight, which consist of ~ 200 wind turbines in the upwind direction for wind direction south 190°, showed that the wake length (which is defined as the distance with the velocity deficit of the wind farm wake larger than 0.1 m/s) varies from several kilometers to more than 50 kms as reported by Platis et al. (2018). It should be noted that there is no generally accepted definition for the wake length of wind farm. For example, Platis et al. (2021) and Maas and Raasch (2022) defined the wake length as the distance where the wake velocity recovery to 95% and 90% of inflow, respectively. Besides the velocity deficit in the wake, the measurements also showed significant impacts of the wind farm on the potential temperature and water vapor at even 60 km downwind for strong stable stratification cases (Siedersleben et al. 2018). Using the aircraft measurements, the entrainment length scales above and downstream of the farms in German Bight were also investigated by Syed et al. (2022), showing increased intensity of small-scale turbulence. Measurements of wind farms located in German Bight using long-range-scanning Doppler wind LiDAR (Light Detection And Ranging) were also carried out (Cañadillas et al. 2022). The results showed that the wind farm wakes are more pronounced under stable atmospheric conditions when compared with unstable atmospheric conditions. Wind tunnel measurement is an effective means of analyzing the flow around a simulated wind farm. Chamorro and Porté-Agel (2010) measured the flow within wind farms for two different streamwise turbine spacings in a wind tunnel. And, they found that wind farms with larger streamwise turbine spacings have better performance. The effect of non-uniform streamwise turbine spacing on wind farm performance was explored by Bossuyt et al. (2018) via wind tunnel experiments. Similar distributions of turbulent shear statistics in the streamwise direction were observed by Chamorro et al. (2011) for wind farms with different turbine spacings (e.g., $S_x = 5$ and 7 rotor diameters).

Wakes of utility-scale wind farms were simulated using computational models of different levels of fidelity from mesoscale weather forecasting models to large-eddy simulation (LES). Simulations of the wind farms in German Bight using the Weather Research and Forecasting (WRF) model, in which the effects of wind farms on the extraction of mean kinetic energy (MKE) and the generation of turbulence are parameterized, were carried out by Siedersleben et al. (2018), Platis et al. (2021) and Cañadillas et al. (2022). In the work by Siedersleben et al. (2018), the predicted potential temperature and the water vapor mixing ratio of the wind farm wake were in good agreement with the aircraft measurements. Good agreements in wind speed were observed for neutral and unstable atmospheric conditions, while large discrepancies in wind speed were observed for stable conditions (Cañadillas et al. 2022).

That the mesoscale model may not accurately reproduce the atmospheric condition was also reported by Platis et al. (2021). LESs of hypothetical wind farms in the German Bight with $\sim$ 1000 and $\sim$ 2000 wind turbines were carried out by Maas and Raasch (2022). They found that the wake length can be greater than 100 km for the wind farm with a small turbine spacing, i.e., $S_x = 5D$ compared to $7D$, under shallow boundary layers.

Flow statistics of wakes of idealized wind farms, in which the complexity of real-life wind farms (e.g., varying wind conditions and wind turbine operational conditions) was simplified, were investigated using LES. Maas (2022) simulated wakes of a small wind farm of rated capacity 0.96 GW and a large wind farm of rated capacity 11.52 GW. Their results showed that the wake lengths with significant turbulence intensity are close for the two farms, while the magnitude of the inertial gravity wave triggered by the large wind farm is significantly larger.

LES of the wake of a wind farm consisting of 40 wind turbines was carried out by Dong et al. (2022), showing that the velocity in the wake recovers to 95% of the freestream incoming wind speed at 55 rotor diameters downstream from its last row. Stieren and Stevens (2022) employed LES to study the interaction of two adjacent wind farms under a neutral atmospheric boundary layer. Their results showed that the wake from the upstream wind farm affects the flow within and around the downstream wind farm. It was also observed that the velocity deficit in the wake of the wind farm with staggered wind turbines was stronger than that with aligned wind turbines.

Other computational studies of wind farm flows have also been carried out in the literature with a focus on the wind farm itself (instead of wind farm wakes). Large-eddy simulations of infinitely large wind farms (lengths exceeding the atmospheric boundary layer by an order of magnitude) have been carried out in early studies (Calaf et al. 2010; Yang et al. 2012; Meyers and Meneveau 2012). For instance, different effects of streamwise and spanwise spacings were shown by Yang et al. (2012), with an effective roughness height model proposed accounting for the different effects. The placement of wind turbines affects the performance of wind farms. A staggered configuration (in the spanwise direction) is often more efficient in energy extraction when compared to the aligned one (Wu and Porté-Agel 2013). Zhang et al. (2019) simulated infinitely large wind farms with LES and found that the staggered-in-vertical configuration affects the power in the entrance area of the wind farm, but has almost no effect on the vertical kinetic energy transport in the fully developed region.

Engineering models play an important role in wind energy applications. Evaluations of engineering models for wind farm wakes have been carried out by several authors. Platis et al. (2021) evaluated the analytical model proposed by Emeis (2010), which modeled the wind farm as a whole (top-down approach) and assumed the wake recovers in an exponential way, using in situ data and mesoscale simulation results. The obtained results are comparable to the observations, with the effect of wind farm layout and the MKE fluxes from the sides of a wind farm yet to be taken into account. The existing top-down analysis models often only consider the neutral atmospheric condition, and cannot account for the heterogeneous effect of wind farm layout for different wind directions (Porté-Agel et al. 2020). Stieren and Stevens (2021) evaluated several bottom-up models, which predict wind farm wakes via modeling the wake from each wind turbine, using LES data of two idealized wind farms (each with 72 wind turbines, 10 km apart under a neutral boundary layer), and observed over estimations of the velocity recovery for all the considered models.

To develop engineering models for wind farm wakes, it is essential to understand the influence mechanism of different factors. Because of the unknowns (e.g., the wind turbine blade design, power curve) and many factors (wind speed and direction, atmospheric condition, wind farm layout) involved in the wake development of a utility-scale wind farm, it is difficult

to quantify the role of different factors using in situ data. With numerical simulations, the wake dynamics of a wind farm under the control of a specific parameter can be investigated. The streamwise wind turbine spacing, number of turbine rows and surface roughness all affect the performance of a wind farm (Stevens et al. 2016; Stevens 2016; Kim and Lim 2017), but their effects on the wake of a wind farm are yet to be fully understood.

In this work, we simulates six wind farms for different streamwise turbine spacings, number of rows, and ground surface roughness lengths, using LES with wind turbines parameterized using the actuator disk model. To simplify the problem, only neutral atmospheric condition is considered. The Coriolis force is not considered so that the wind direction remains the same at all the vertical positions. The internal gravity wave is not considered either because of the assumption of neutral stratification condition, although it was shown that it can cause power dissipation for large-scale wind farms (Allaerts and Meyers 2018, 2019; Maas 2022).

The inflows are fully developed, which are generated from two precursory simulations with the roughness length of ground surface $k_0 = 0.001$ m and 0.1 m, being representative of a typical surface roughness of offshore conditions (Lamare et al. 2023; McCarty and Churnside 2016; Pratt 1980; Ma et al. 2021) for the former and of a cultivated area for the latter, respectively. In the precursory simulations, the flow is driven by pressure gradient to maintain a constant mass flow rate, with periodic boundary conditions applied in the horizontal directions and the boundary conditions at the bottom and top boundaries the same as the wind farm wake simulations. The friction velocity $u^*/U_{hub} = 0.038, 0.066$ for the inflow $k_0 = 0.001$ m and 0.1 m, respectively.

The rest of the paper is organized as follows: Sect. 2 describes the employed numerical method; Sects. 3 and 4 present the computational setup of the simulated cases, and the analysis of the obtained simulation results, respectively; Sect. 5 summarizes the findings from this study.

2 Numerical Method

In this work, the wind farm wake is simulated using LES with an actuator disk model for wind turbine aerodynamics. The LES module of the VFS-Wind code (Yang et al. 2015, a; Calderer et al. 2015) is employed for carrying out the simulations. The governing equations are the filtered incompressible Navier-Stokes equations in Cartesian coordinates,

$$\frac{\partial u_i}{\partial x_i} = 0, \tag{1}$$

$$\frac{\partial u_i}{\partial t} = -\frac{\partial u_i u_j}{\partial x_j} - \frac{1}{\rho}\frac{\partial p}{\partial x_i} - \frac{1}{\rho}\frac{\tau_{ij}}{\partial x_j} + \frac{\mu}{\rho}\frac{\partial^2 u_i}{\partial x_j \partial x_j} + f_i, \tag{2}$$

where $i, j = \{1, 2, 3\}$, respectively, are the tensor indices, x_i are the Cartesian coordinates, u_i is the velocity in Cartesian coordinates, μ denotes the dynamic viscosity, ρ is the fluid density, p is the pressure, and f_i are body forces introduced by the actuator disk model, τ_{ij} is the subgrid-scale (SGS) stress, modeled using the dynamic Smagorinsky model (Germano et al. 1991).

To model the wind turbine aerodynamics, the actuator disk (AD) model is employed. The AD represents the swept area of the wind turbine rotor. The thrust of the rotor is modeled by a distributed force on the AD (Jimenez et al. 2007). Although the AD model cannot predict the tip vortices of the blade, but its prediction accuracy of velocity deficit is acceptable especially

for turbulent flows (Li et al. 2022). Considering rotation and the force distribution in the radial direction was found increasing the predictive capability of the AD model (Porté-Agel et al. 2011; Dong et al. 2022). As the focus of this work is on the wind farm wake (which is significantly longer than the wind turbine wake), for which the rotation of a wind turbine's wake decays completely, the AD model without rotation is employed in this work.

In the employed the actuator disk model, the rotor is modeled with the thrust (T) uniformly distributed on a disk, which is computed as follows:

$$T = \frac{1}{2}\rho C_T A U_{in}^2, \tag{3}$$

where $C_T = 4a(1-a)$ (a is the axial induction factor) from one-dimensional momentum theory, $A = \pi D^2/4$ is the rotor-swept area, and $U_{in} = U_d/(1-a)$ (in which U_d is the streamwise velocity averaged over the disk). Two sets of grids are employed in the AD simulations, i.e., the Cartesion or curvilinear background grid for the fluid flow simulations and the triangular grid for the actuator disk. To obtain disk-averaged streamwise velocity U_d, the velocity at the center of the triangular cell of the actuator disk mesh is interpolated from the background volume grid. The thrust on the rotor can then be obtained with U_d. At last, the obtained thrust is distributed to the background grid to advance the flow field in time. The velocity interpolation and the force distribution are performed using the discrete delta functions (Yang et al. 2009, 2012).

The governing equations are discretized in space using a second-order accurate central differencing scheme and advanced in time using a second-order fractional step method (Ge and Sotiropoulos 2007). The momentum equation is solved with a Jacobian-Free Newton-Krylov method. The Poisson equation is solved with a Generalized Minimal Residual (GMRES) method with an algebraic multigrid acceleration.

3 Case Setup

The computational setup of the simulations wind farms is described in this section.

The axial induction factor is $a = 0.25$ for all the turbines. The incoming wind speed at hub height is 8.5 m/s. Figure 1 shows the computational domain of the simulated cases. The simulated wind farms consists of 30, 50 and 100 turbines, arranging in 3, 5 and 10 rows (N_{row}), respectively, and 10 columns (N_{col}) in parallel, with a spacing of $5D$ in the spanwise direction. The hub height and rotor diameter of the simulated wind turbine is $D = z_{hub} = 100$ m. The streamwise turbine spacings are $6D$ (WF A), $8D$ (WF B, WF D, WF E, WF F), and $10D$ (WF C) for the six wind farms. The schematic of the wind farm layout is shown in Table 1. The employed turbine spacings and number of wind turbines are in the range of typical utility-scale wind farms, for instance, the Horns Rev wind farm with a mean turbine spacing of $8D$, and the Nysted wind farm with turbine spacing $10.5D$ east–west and $5.8D$ north–south. The size of the computational domain is $(151D; 167D; 225D) \times 95D \times 10D$ discretized using number of grid nodes $(756; 836; 1126) \times 951 \times 152$ in the streamwise, spanwise and vertical directions, respectively. In the vertical direction, the grid is uniformly distributed in the near-ground region ($z < 1.5D$) with vertical grid spacing $\triangle z = D/50$. Then $\triangle z$ gradually increases as moving away from the ground. In wind farm simulations, the grid spacing of $D/20$ in the vertical direction is shown enough to capture the key flow dynamics (Yang et al. 2012). In the streamwise and spanwise directions, the grid spacings are $\triangle x = D/5$ and $\triangle y = D/10$, respectively.

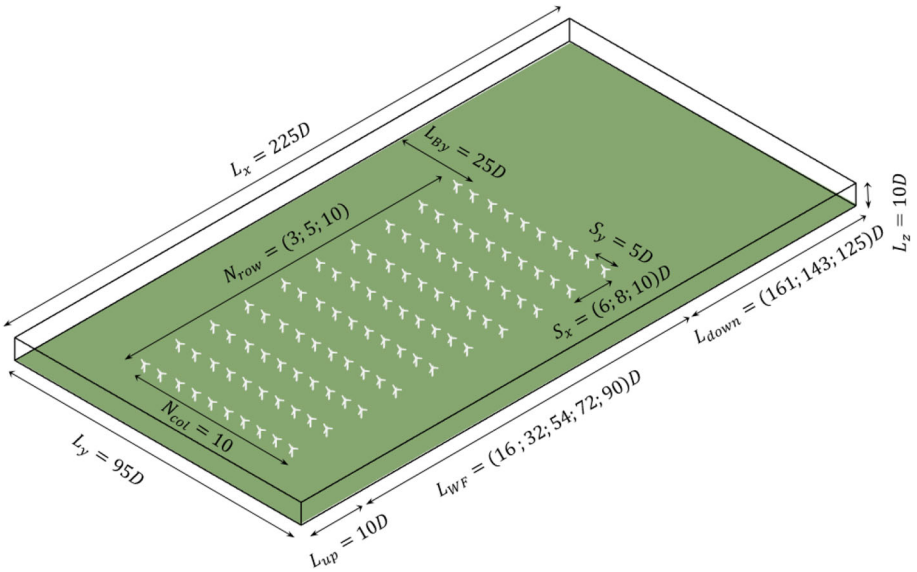

Fig. 1 Schematic of the computational domain for wake simulations of the six wind farms with different streamwise turbine spacings, numbers of turbine rows and surface roughness lengths of ground surface, respectively. And the figure is not to scale because it is difficult to keep the physical ratios

Table 1 Case setups of the six simulated wind farms

Case name	S_x	S_y	N_{row}	N_{col}	L_{WF}	L_{down}	k_0 (m)	z_{hub}
WF A	6D	5D	10	10	54D	161D	0.001	1D
WF B	8D	5D	10	10	72D	143D	0.001	1D
WF C	10D	5D	10	10	90D	125D	0.001	1D
WF D	8D	5D	5	10	32D	125D	0.001	1D
WF E	8D	5D	3	10	16D	125D	0.001	1D
WF F	8D	5D	10	10	72D	143D	0.1	1D

At the bottom wall, the wall shear stress is applied, which is computed using the velocity at the first off-wall grid node and the logarithmic law of the form $u/u^* = \frac{1}{\kappa}\ln(z/k_0)$ (where $u^* \equiv \sqrt{\tau_w/\rho}$, is the friction velocity, τ_w is the wall shear stress, $\kappa = 0.4$ is the Kármán constant and k_0 is the roughness length). At the top and spanwise boundaries, the free-slip boundary condition is applied. At the outlet, the Neumann boundary condition is employed. At the inlet, the fully developed turbulent flow generated from the precursory simulation is applied.

Figure 2a, b, c show the mean streamwise velocity, streamwise Reynolds normal stress, and Reynolds shear stress of the inflow, respectively. The inflow is generated from the precursory simulation, in which the boundary conditions at the top and the bottom are the same as the wind farm simulations. In the horizontal directions, the periodic boundary conditions are applied. The time step of the simulation is $0.086D/U_{hub}$ (~ 1 s), where U_{hub} is the inflow mean streamwise velocity at hub height. A flow-through requires approximately 3,000 time steps for the longest computational domain. Initially, 4,000 time (~ 1.1 h) steps were carried

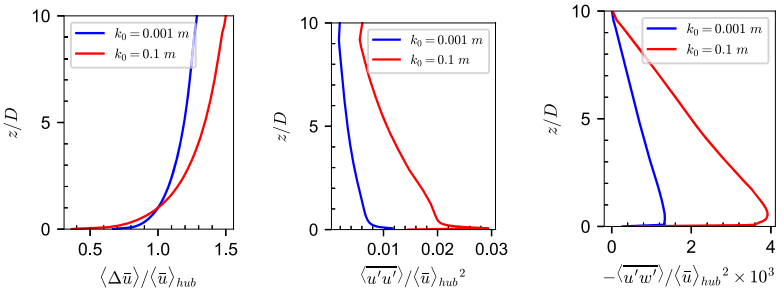

(a) Inflow velocity (b) Inflow turbulence level (c) Inflow turbulent shear

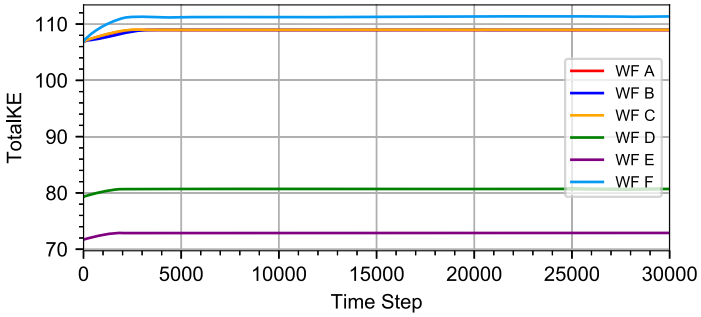

(d) The TotalKEs of the six wind farm cases, which are statistically steady after 4000 steps.

Fig. 2 The inflow (which is applied at 10D upstream of the first row of the wind farm) and the criterion for the flow to reach full developed

out to obtain a fully developed state by examining the value of the total kinetic energy, as shown in Fig. 2d. The total kinetic energy (TotalKE) is defined as the sum of kinetic energy of all grids in the whole computational domain:

$$TotalKE = \sum_{i=0}^{N_i} \sum_{j=0}^{N_j} \sum_{k=0}^{N_k} u_{ijk}^2 + v_{ijk}^2 + w_{ijk}^2, \tag{4}$$

where N_i, N_j and N_k are the number of grids in the i, j, and k directions, respectively, and u_{ijk}, v_{ijk} and w_{ijk} are the Cartesian velocity components computed at cell centers. Then, 26,000 time steps (~ 7.3 h) are continued for temporal averaging to obtain the flow statistics.

4 Results

This section presents the analysis of the wind farm simulation results. Before examining the characteristics of wind farm wakes, we firstly examine the power output in Fig. 3.

It is seen in Fig. 3 that the power drops significantly at the second row and remains at approximately the level at the following rows. A "fully developed state" in terms of power output is quickly reached for all the three wind farms, with the corresponding power output higher for cases with larger streamwise turbine spacing, being consistent with the previous research results (Stevens et al. 2016).

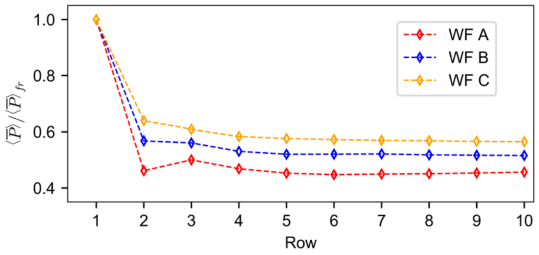

Fig. 3 Time-averaged power of wind turbines in different rows of the three wind farms. The power of the first row $\langle\overline{P}\rangle_{fr}$ is employed for normalization

4.1 Mean Velocity and Turbulence Statistics

4.1.1 Effects of Different Wind Turbine Spacings

In this paper, u, v, w and $\bar{u}, \bar{v}, \bar{w}$ denote the instantaneous and the corresponding time-averaged velocity, respectively. The $u' = u - \bar{u}$ (the same for the other two components) denotes the temporal velocity fluctuations. The $\bar{\cdot}$ and $\langle\cdot\rangle$ represent the time averaging and the spanwise averaging (from $y_{2c} - 2.5D$ to $y_{9c} + 2.5D$, where y_{2c} and y_{9c} denote the spanwise coordinate of the turbines in the second and ninth column, respectively) of physical quantities. The $u'' = u - \langle u\rangle$ (the same for the other two components) denotes the spatial velocity fluctuations.

The mean inflow velocities are employed for normalization, including the $\bar{u}_{in}(y, z)$ and the $\langle\bar{u}\rangle_{hub}$. The $\bar{u}_{in}(y, z)$ is time-averaged streamwise velocity $\bar{u}$ at the inlet (which is $10D$ upstream of the first row of wind turbines in the wind farm). And the $\langle\bar{u}\rangle_{hub}$ is calculated by further averaging $\bar{u}_{in}(y, z_h)$ at hub height in the spanwise direction. In Fig. 4b, d, f, the $\bar{u}_{in}$ at the corresponding spanwise location is employed for normalization. The velocity deficit is defined as the difference between the streamwise velocity at the inlet and that at different streamwise locations, i.e., $\Delta\bar{u} = \bar{u}_{in} - \bar{u}$. Figure 4a, c, e show the velocity deficit in the hub-height plane for the three wind farms. As seen, the velocity deficit persists for a very long distance in the wake of the three wind farms. It is noticed that the velocity deficit is confined to a region with its width close to the width of the wind farm, being in agreement with Dong et al. (2022) and Stieren and Stevens (2022). The width of the velocity deficit is defined as the spanwise positions where $\Delta\bar{u}/\langle\bar{u}\rangle_{hub} = 1\%$ (the value is artificially selected, and it is considered that the velocity deficit less than this value can be ignored) at different streamwise locations in the above figure, and the black dash-dotted lines visualize it. The result indicates insignificant momentum transport of the wind farm wake in the spanwise direction, which will be employed to simplify the subsequent kinetic energy analysis of the wind farm wake.

Figure 4b, d and f show the velocity deficit in the vertical $x - z$ plane located at the middle of the wind farm ($y = 45D$) to demonstrate the impact of the wind farm on the distribution of streamwise velocity in the vertical direction. The black dotted lines indicate the top boundary below which the wind is affected by the wind farm. It is seen that the vertical extent of this velocity-deficit region gradually increases at further wind farm downstream locations (to approximately $5D$ above the ground at $100D$ downstream of the farm), indicating the momentum mixing between the wake and the above atmospheric flows. The red dash-dotted lines represent the vertical position for the maximum velocity deficit, which is located around z_{hub} inside the farm and near $z_{top} = z/D = 1.5$ at most farm downstream locations. The fluctuation is mainly caused by the difficulty of identifying the vertical position of the maximum velocity deficit especially at far wake positions. Different methods (e.g., those in

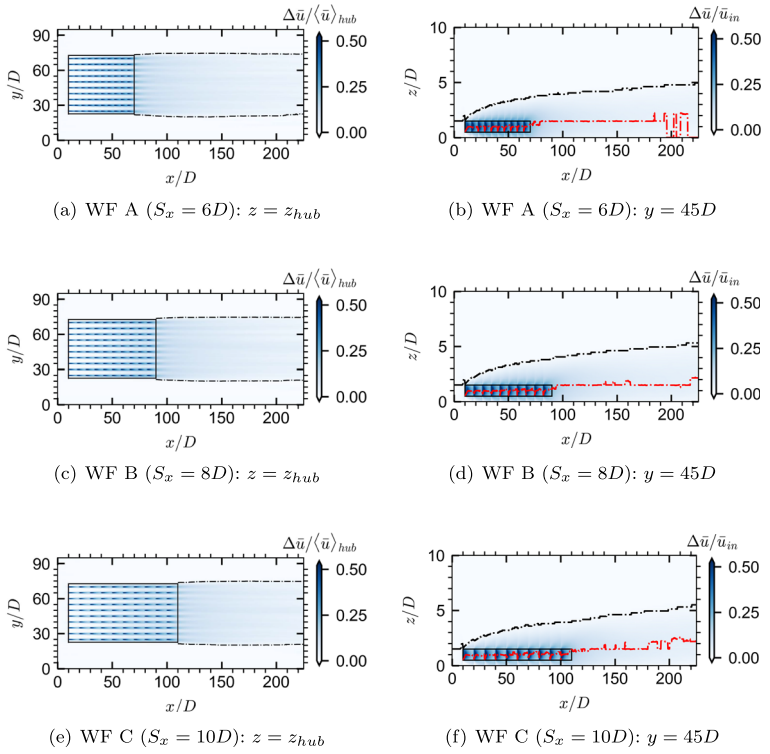

(a) WF A ($S_x = 6D$): $z = z_{hub}$ (b) WF A ($S_x = 6D$): $y = 45D$

(c) WF B ($S_x = 8D$): $z = z_{hub}$ (d) WF B ($S_x = 8D$): $y = 45D$

(e) WF C ($S_x = 10D$): $z = z_{hub}$ (f) WF C ($S_x = 10D$): $y = 45D$

Fig. 4 Contours of time-averaged streamwise velocity deficit for the three simulated wind farms. The black solid line encloses the region with the wind farm (including the S_x distance downstream of the last row of wind turbines). In **a**, **c**, **e**, the black dash-dotted lines show the spanwise positions where $\Delta\bar{u}/\langle\bar{u}\rangle_{hub} = 1\%$ at different streamwise locations. In **b**, **d**, **f**, the black dash-dotted lines and the red dash-dotted lines show the vertical position where $\Delta\bar{u}/\bar{u}_{in} = 1\%$ and for the maximum of $\Delta\bar{u}/\bar{u}_{in}$ at different streamwise locations, respectively.It is noted that the horizontal and vertical axes are not scaled in the same way

Ning and Wan (2019) and Feng et al. (2022)) for identifying wake locations can be examined for the far wake of a wind farm in the future work. The vertical position of a wind farm wake is crucial for analyzing the wake effect on power output of downstream wind farms. And such vertical variation of wake position is yet to be accounted for in engineering models.

Figure 5a, c and e show the contours of the vertical velocity. Within the farm, it is seen that the flow at the top tip position is featured by an upward motion as approaching a turbine, and a downward motion is in its wake. In the wake of the farm, the flow is characterized by a downward motion especially in its immediate downstream where the magnitude of the vertical velocity is maximized. Its role on the wake recovery of the farm will be analyzed in the rest of the paper.

Figure 5b, d and f show the contour of the spanwise-averaged pressure. It is seen that the streamwise pressure difference dominates the near-turbine region as expected, which is directly related with the thrust on rotor. As the focus of the paper is on the wind farm wake, the effect of pressure difference on the energy transport in the vertical direction can be neglected, because the pressure is almost uniform distributed in the wind farm wake.

Figure 6 shows the three components of the normal stresses and the primary shear stresses including Reynolds stress and dispersive stress for WF C (which is consistent with WF B and

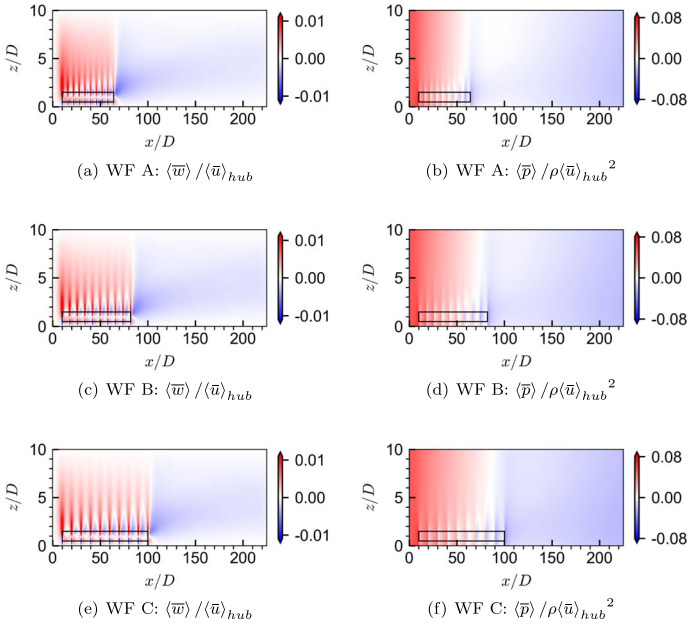

Fig. 5 Contours of time- and spanwise-averaged vertical velocity and pressure for the three wind farms WF A, B and C. The black solid line encloses the region with the wind farm. It is noted that the horizontal and vertical axes are not scaled in the same way

WF A). As seen, the magnitudes of Reynolds stresses are significant for the entire wake in comparison with the dispersive stresses, which are only observed in the near-turbine region. In addition, the Reynolds shear stress $\left\langle\overline{u'w'}\right\rangle$ influences a large region of the wind farm wake, which was shown playing an important role in the velocity recovery within large wind farms (Calaf et al. 2010; Stevens and Meneveau 2017).

After showing the overall simulated flow field, Fig. 7 shows the velocity deficit $(\Delta\bar{u}/\langle\bar{u}\rangle_{hub})$ at locations relative to the downstream end of the wind farm (x_{lr}), positioned in the hub plane. It is seen that the features of turbine columns are identifiable only in wind farm's near wake locations (e.g., $x - x_{lr} < 20D$), and gradually diminish at further downstream locations (e.g., $x - x_{lr} = 50D$). As for the magnitude of velocity deficit, it decreases to approximately 5% (the selection of threshold refers to Dong et al. (2022)) of the $\langle\bar{u}\rangle_{hub}$ at $x - x_{lr} = 90D$. One important observation is that the wake velocity deficits of the three wind farms are approximately the same at the same $x - x_{lr}$ locations, implying that the streamwise turbine spacing has a negligible effect on the wind farm wake at the same $x - x_{lr}$ locations for the simulated cases. Figure 8 shows the turbulence intensity $\sigma_u/\langle\bar{u}\rangle_{hub}$ at locations relative to the downstream end of the wind farm x_{lr}, positioned in the hub plane. The most notable phenomenon is that the wake of the wind farm is accompanied by turbulence intensity higher than the incoming flow level, which lasts for a distance of more than 110D, and gradually weakens with the farm's downstream distance (Stieren and Stevens 2022; Maas and Raasch 2022; Maas 2022). It is also found that the turbulence intensity of the wakes of the three wind farms is almost the same at the same $x - x_{lr}$ location.

Figure 9 shows the streamwise variations of the spanwise-averaged velocity deficit $\langle\Delta\bar{u}\rangle/\langle\bar{u}\rangle_{hub}$ and turbulence intensity $\langle\sigma_u\rangle/\langle\bar{u}\rangle_{hub}$. These two quantities are exponentially

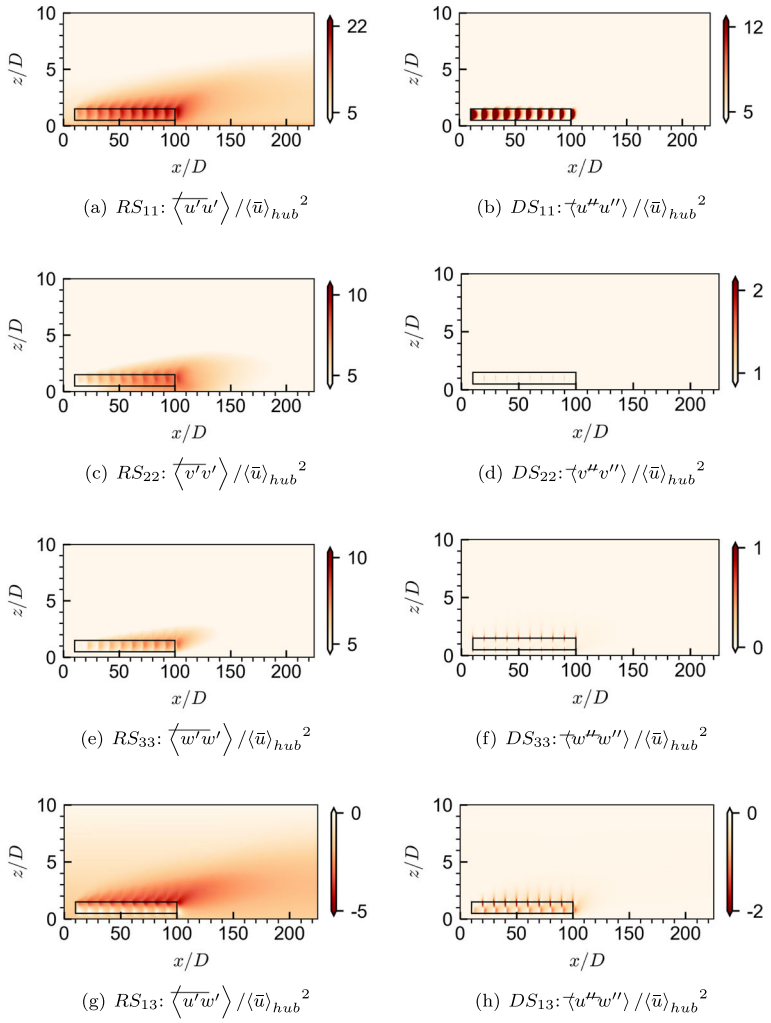

(a) RS_{11}: $\left\langle \overline{u'u'} \right\rangle / \langle \bar{u} \rangle_{hub}{}^2$ (b) DS_{11}: $\langle \bar{u}''\bar{u}'' \rangle / \langle \bar{u} \rangle_{hub}{}^2$

(c) RS_{22}: $\left\langle \overline{v'v'} \right\rangle / \langle \bar{u} \rangle_{hub}{}^2$ (d) DS_{22}: $\langle \bar{v}''\bar{v}'' \rangle / \langle \bar{u} \rangle_{hub}{}^2$

(e) RS_{33}: $\left\langle \overline{w'w'} \right\rangle / \langle \bar{u} \rangle_{hub}{}^2$ (f) DS_{33}: $\langle \bar{w}''\bar{w}'' \rangle / \langle \bar{u} \rangle_{hub}{}^2$

(g) RS_{13}: $\left\langle \overline{u'w'} \right\rangle / \langle \bar{u} \rangle_{hub}{}^2$ (h) DS_{13}: $\langle \bar{u}''\bar{w}'' \rangle / \langle \bar{u} \rangle_{hub}{}^2$

Fig. 6 Spanwise-averaged Reynolds stresses (RS) and dispersive stresses (DS) for WF C. The plotted quantities are multiplied by a factor of 1000. The black solid line encloses the region with the wind farm. It is noted that the horizontal and vertical axes are not scaled in the same way

fitted, which is selected to be consistent with the form of the analytical model Emeis (2010) and the condition that $\langle \Delta\bar{u} \rangle = 0$ at infinite large distances. However, it should be noted that a linear fit can serve as an acceptable approximation as well. Platis et al. (2021) also showed that the wake velocity of offshore wind farms decreases exponentially as examined via a fitting function. Maas (2022) showed that the size of the wind farm did not affect the attenuation of turbulence intensity. The trends for the three wind farms are approximately the same for both $\langle \Delta\bar{u} \rangle$ and $\langle \sigma_u \rangle$ except for $\langle \sigma_u \rangle$ near the downstream end of the wind farm ($x - x_{lr} < 20D$). The comparison of the two plots reveals that the velocity recovery rate is higher than the decay rate of wake turbulence. This indicates that one needs to examine both the velocity deficit and wake turbulence in order to determine whether the wake has fully recovered to the inflow state or not (Churchfield et al. 2012; Maas 2022). Vertical variations

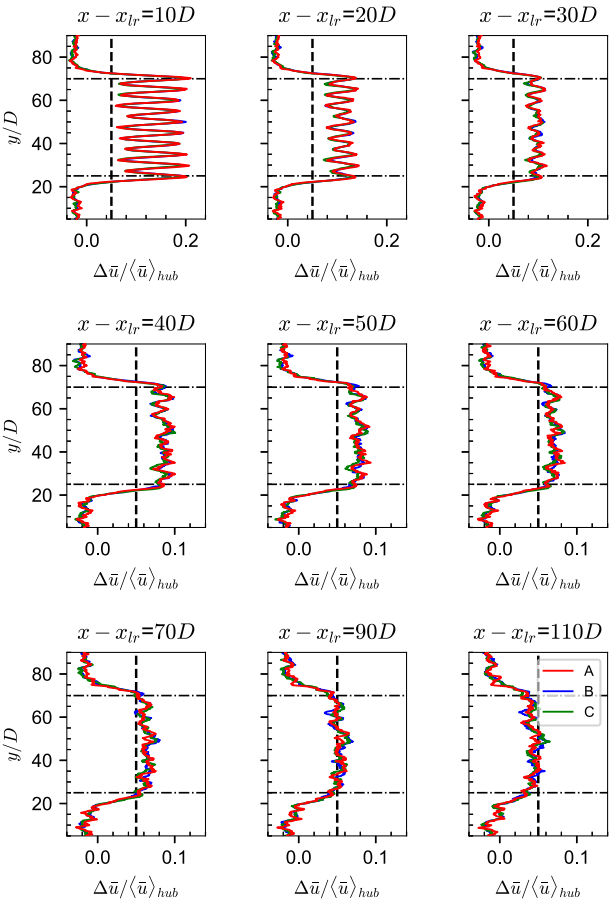

Fig. 7 Spanwise profiles of the time-averaged velocity deficit at hub height for different downstream positions relative to the last-row wind turbines located at x_{lr}. The lines with 'A', 'B' and 'C' in legend represent WF A, B and C, respectively. The vertical black dashed line corresponds to $\Delta\bar{u}/\langle\bar{u}\rangle_{hub} = 0.05$. The black dotted-dash lines represent the spanwise boundaries of the wind farms

of spanwise-averaged wake statistics are shown in Fig. 10. As seen in Fig. 10a, the streamwise velocities $\langle\bar{u}\rangle$ from cases with different turbine spacings are almost identical at all the considered vertical positions. As for the streamwise component of Reynolds stresses $\left\langle\overline{u'u'}\right\rangle$ and the Reynolds shear stress $-\left\langle\overline{u'w'}\right\rangle$ shown in Fig. 10b, c, the vertical positions for the maximum wake-induced $\left\langle\overline{u'u'}\right\rangle$ and $-\left\langle\overline{u'w'}\right\rangle$ move upward with the wake-influenced region widened in the vertical direction as one travels in the downstream direction. Different from $\langle\bar{u}\rangle$, the magnitudes of $\left\langle\overline{u'u'}\right\rangle$ and $-\left\langle\overline{u'w'}\right\rangle$ from the cases with larger streamwise turbine spacings are somewhat higher in the region near the top boundary of the wake-influenced region. For the magnitudes of $\left\langle\overline{u'u'}\right\rangle$ at $x - x_{lr} = 10D$, case C is up to 27.6% higher than case A, and case B is up to 16.1% higher than case A. As for the magnitudes of $-\left\langle\overline{u'w'}\right\rangle$ at

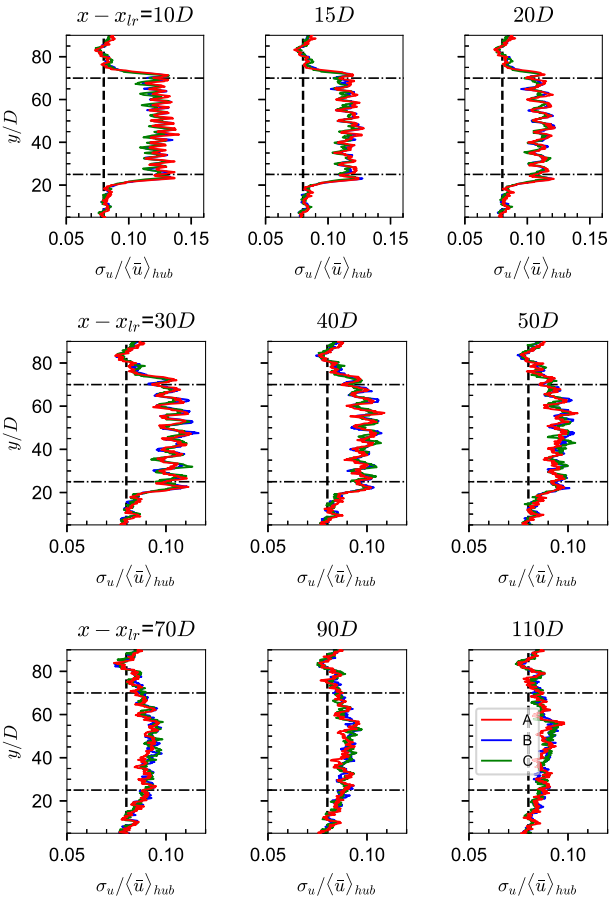

Fig. 8 Spanwise profiles of the time-averaged turbulence intensity at hub height for different downstream positions relative to the last-row wind turbines located at x_{lr}. The lines with 'A', 'B' and 'C' in legend represent WF A, B and C, respectively. The vertical black dashed line corresponds to $\sigma_u/\langle\bar{u}\rangle_{hub} = 0.080$, which represents the turbulence intensity of the incoming flow. The black dotted-dash lines represent the spanwise boundaries of the wind farms

$x - x_{lr} = 10D$, case C is up to 34.6% higher than case A, and case B is up to 18.8% higher than case A.

So far, we have seen that the streamwise turbine spacing significantly affects the power output of turbines in different rows, but has marginal effect on the statistics of wind farm wakes at far-wake locations. Analyses of the influence of the number of rows of wind turbines and the roughness length of ground surface on the wake flow of the wind farms are shown in Sects. 4.1.2 and 4.1.3, respectively.

4.1.2 Effects of Number of Wind Turbine Rows

Figure 11 shows the wind farm wake velocity deficits $\Delta\bar{u}/\langle\bar{u}\rangle_{hub}$ in the hub plane for wind farms with different numbers of rows of wind turbines. At the same position $(x - x_{lr})$ downstream of the wind farm, the magnitudes of velocity deficits are smaller for cases with

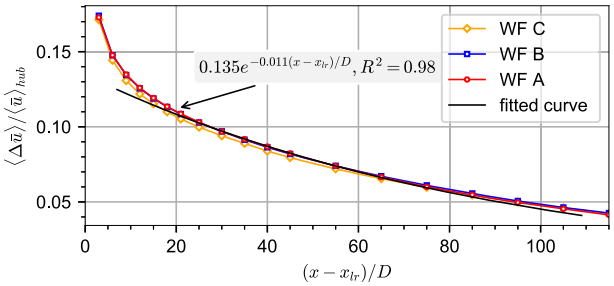

(a) Streamwise velocity deficit: $\langle \Delta\bar{u} \rangle / \langle \bar{u} \rangle_{hub}$

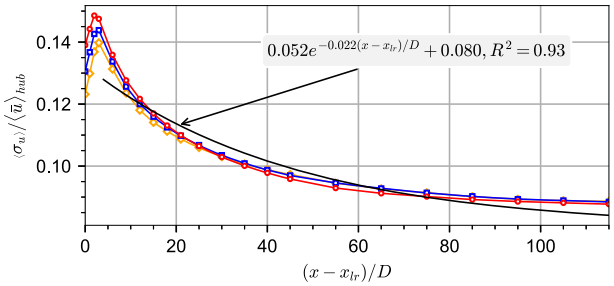

(b) Turbulence intensity: $\langle \sigma_u \rangle / \langle \bar{u} \rangle_{hub}$

Fig. 9 Time and spanwise-averaged velocity deficit and turbulence intensity in the wake of the three wind farms in the hub-height plane. The lines with markers in red, blue and orange represent WF A, B and C, respectively. The black solid lines show the curve fitting results, which are obtained accounting for the assumptions that $\langle \Delta\bar{u} \rangle$ approaches zero and $\langle \sigma_u \rangle$ reduces to that of the inflow at infinite large distances, where R^2 means goodness of fit

fewer rows of wind turbines. Such difference decreases with the downstream distance (e.g., $x - x_{lr} = 10D, 110D$), which indicates a faster velocity recovery for the wind farm with a larger number of rows of wind turbines, which was also demonstrated in a previous study by Maas (2022). Moreover, the interaction of wake columns in the spanwise direction is stronger for the wind farm with more rows of wind turbines, causing the wake column characteristics to disappear earlier (e.g., the wake column characteristics are still present at $x - x_{lr} = 50D$ for both WF D and E, but disappear for WF B at the same location). Figure 12 shows the spanwise profiles of the turbulence intensity $\sigma_u / \langle \bar{u} \rangle_{hub}$. Higher levels of turbulence intensity (e.g., $x - x_{lr} = 40D$) are observed for wind farms with more rows of wind turbines. Vertical profiles of spanwise-averaged wake statistics are shown in Fig. 13. It is seen the vertical region influenced by the wind farm wake is larger for wind farms with more rows of wind turbines for both the streamwise velocity and turbulence statistics.

Overall, significant effects of the number of wind turbine rows on the wind farm wake statistics are observed.

4.1.3 Effects of Roughness Lengths of Ground Surface

In Fig. 14, the influence of roughness length of ground surface on the velocity deficits $\Delta\bar{u} / \langle \bar{u} \rangle_{hub}$ in wind farm wake is examined. At the same position $(x - x_{lr})$ downstream of the wind farm, the velocity deficits are smaller for the case with larger roughness length of ground surface. As for the turbulence intensity $\sigma_u / \langle \bar{u} \rangle_{hub}$ shown in Fig. 15, higher level of

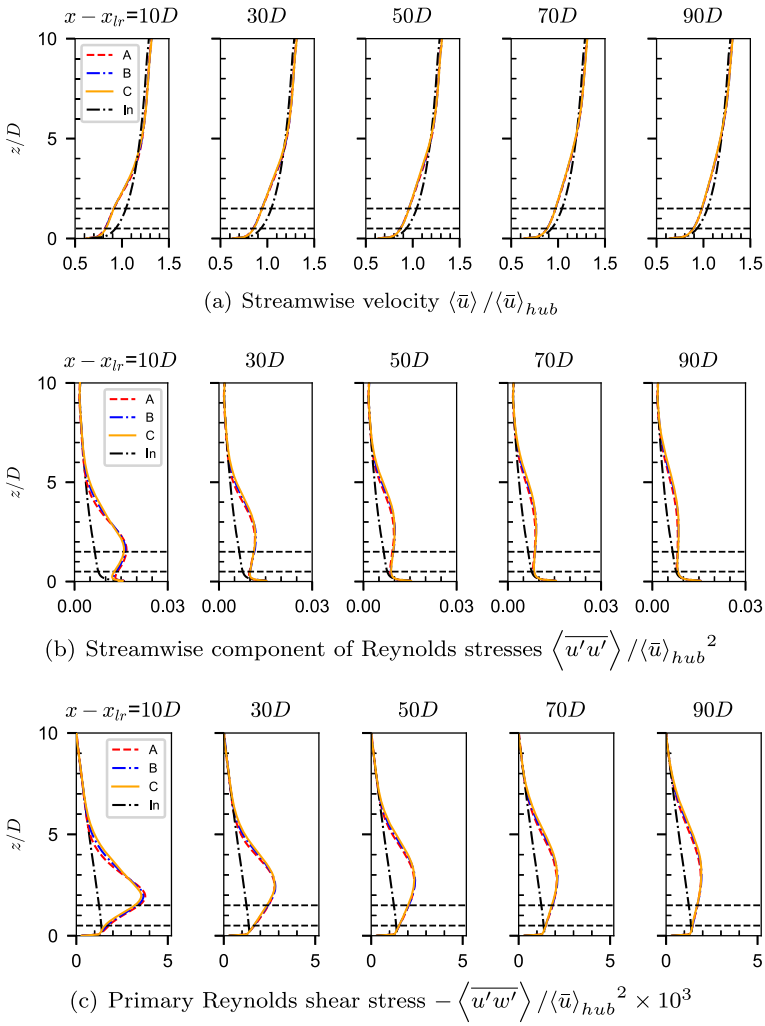

Fig. 10 Vertical profiles of the time- and spanwise-averaged statistics at different downstream locations relative to the last row of the wind farm. The black dashed lines show the top and bottom tips of the wind turbine rotor. The lines with 'A', 'B' and 'C' in legends represent WF A, B and C, respectively. The lines with 'In' in legends show the statistics of the inflow

$\sigma_u/\langle\bar{u}\rangle_{hub}$ is observed for WF F when compared with WF B. Vertical profiles of spanwise-averaged wake statistics for WF B and F are shown in Fig. 16. It is seen the vertical region influenced by the wind farm wake is larger for WF F when compared with WF B for both the streamwise velocity and turbulence statistics.

Overall, it is seen that the roughness length of ground surface is a key factor affecting the wind farm wake statistics.

In the next section, the MKE budget equation is analyzed for velocity recovery in wind farm wakes.

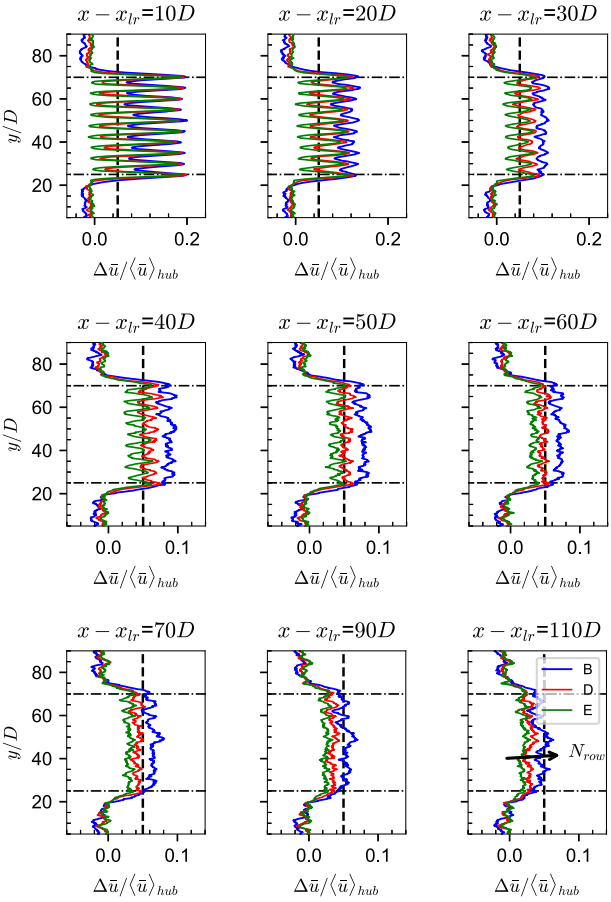

Fig. 11 Spanwise profiles of the time-averaged velocity deficit at hub height for different downstream positions relative to the last-row wind turbines located at x_{lr}. The 'B', 'D' and 'E' in the legend represent WF B, D and E for number of wind turbine rows 10, 5 and 3, respectively. The vertical black dashed line corresponds to $\Delta\bar{u}/\langle\bar{u}\rangle_{hub} = 0.05$. The black dotted-dash lines represent the spanwise boundaries of the wind farms. Arrow with annotation indicates the direction of increase in number of rows

4.2 Analysis of MKE Budget Equation

With the expansion of wake in the spanwise direction, the MKE between wakes of two columns becomes less and less as one travels further in the downstream direction, such that the mixing with the high-momentum fluid above the wake dominates the wake recovery. To understand the process of wake recovery, rather than the turbulent kinetic energy (TKE) transfer processes in the wind farm (Ali et al. 2019), the spanwise-averaged MKE budget equation is employed to analyze the energy transport in the vertical direction.

The MKE budget equation (Pope 2000) is derived from the time- and spanwise-averaged momentum equation in the following form,

$$\frac{\partial \langle\overline{u_i}\rangle}{\partial t} + \frac{\partial \langle\overline{u_i}\rangle \langle\overline{u_j}\rangle}{\partial x_j} = -\frac{1}{\rho}\frac{\partial \langle\bar{p}\rangle}{\partial x_i} - \frac{\partial r_{ij}}{\partial x_j} + \frac{\mu}{\rho}\frac{\partial^2 \langle\overline{u_i}\rangle}{\partial x_j^2} + \langle\overline{f_i}\rangle, \tag{5}$$

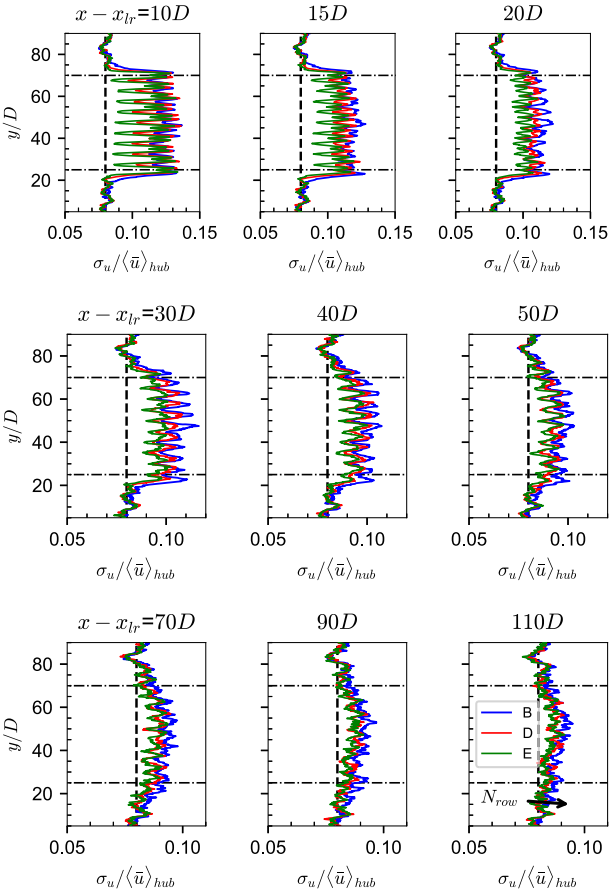

Fig. 12 Spanwise profiles of the time-averaged turbulence intensity at hub height for different downstream positions relative to the last-row wind turbines located at x_{lr}. The 'B', 'D' and 'E' in the legend represent WF B, D and E for number of wind turbine rows 10, 5 and 3, respectively. The vertical black dashed line corresponds to $\sigma_u/\langle\bar{u}\rangle_{hub} = 0.080$, which represents the turbulence intensity of the incoming flow of WF B. The black dotted-dash lines represent the spanwise boundaries of the wind farms. Arrow with annotation indicates the direction of increase in number of rows

where $r_{ij} = \left\langle \overline{u_i' u_j'} \right\rangle + \left\langle \overline{u}_i'' \overline{u}_j'' \right\rangle$. It is noted that the term r_{ij} consists of both Reynolds stress term and dispersive stress term. The volume force $\langle \overline{f_i} \rangle$ is computed as follows:

$$f_i = -\sum_{k=1}^{N_t} T_t / \left(\rho \pi R^2\right) \delta\left(x - x_{c,k}\right) H\left(R_t{}^2 - \left[\left(y - y_{c,k}\right)^2 + \left(z - z_{c,k}\right)^2\right]\right), \tag{6}$$

where H is the Heaviside step function, δ is the Dirac function, N_t is the total number of turbines in the control volume, T_t is the thrust from the AD model, R_t is the rotor radius of wind turbine and the subscript k represents the turbine index. The terms $x_{c,k}$, $y_{c,k}$ and $z_{c,k}$ represent the streamwise, spanwise and vertical rotor center position of the k^{th} wind turbine, respectively.

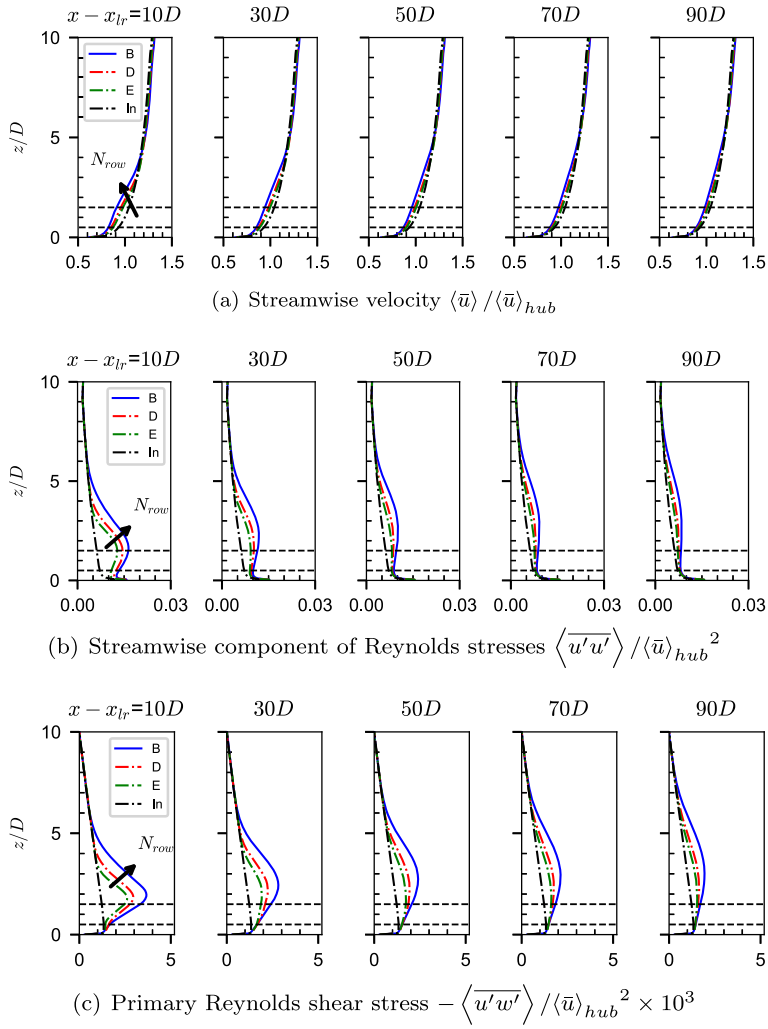

Fig. 13 Vertical profiles of the time- and spanwise-averaged statistics at different downstream locations relative to the last row of the wind farm. The black dashed lines show the top and bottom tips of the wind turbine rotor. The 'B', 'D' and 'E' in the legend represent WF B, D and E for number of wind turbine rows 10, 5 and 3, respectively. The lines with 'In' in legends show the inflow statistics of WF B. Arrows with annotations indicate the direction of increase in number of rows

As the simulated case is statistically steady, the time-derivative term in the momentum equation can be neglected. By neglecting the viscosity effect in the near-wall region, the momentum equation can be further simplified as,

$$\frac{\partial \langle\overline{u_i}\rangle \langle\overline{u_j}\rangle}{\partial x_j} + \frac{1}{\rho}\frac{\partial \langle\overline{p}\rangle}{\partial x_i} + \frac{\partial r_{ij}}{\partial x_j} = \langle\overline{f_i}\rangle. \tag{7}$$

Multiplying both sides of Eq. (7) by $\langle\overline{u_i}\rangle$, the time- and spanwise-averaged MKE budget equation is obtained as follows,

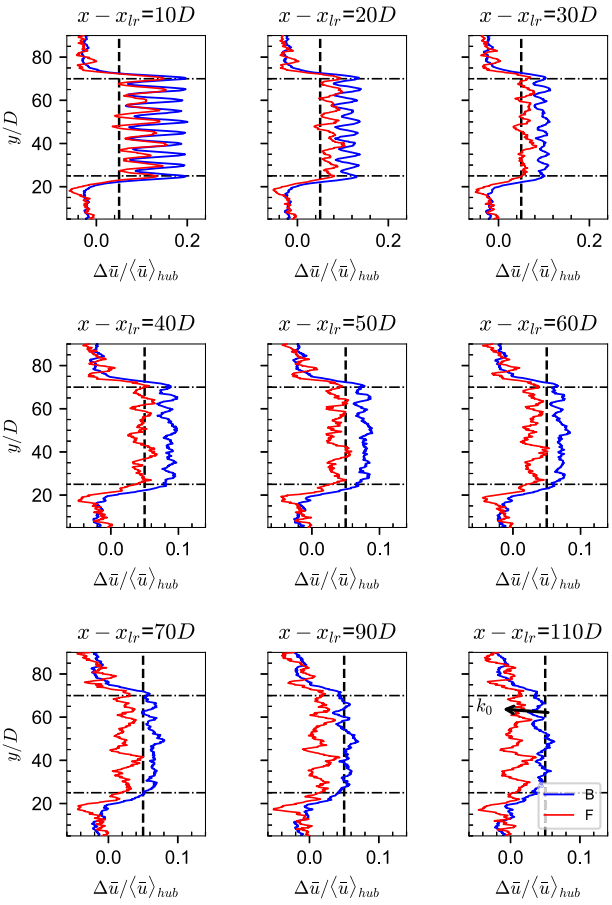

Fig. 14 Spanwise profiles of the time-averaged velocity deficit at hub height for different downstream positions relative to the last-row wind turbines located at x_{lr}. The 'B' and 'F' in the legend represent WF B and F for $k_0 = 0.001$ m and 0.1 m, respectively. The vertical black dashed line corresponds to $\Delta\bar{u}/\langle\bar{u}\rangle_{hub} = 0.05$. The black dotted-dash lines represent the spanwise boundaries of the wind farms. Arrow with annotation indicates the direction of increase in roughness length

$$\langle\overline{u_i}\rangle \frac{\partial \langle\overline{u_i}\rangle \langle\overline{u_j}\rangle}{\partial x_j} + \frac{1}{\rho} \langle\overline{u_i}\rangle \frac{\partial \langle\overline{p}\rangle}{\partial x_i} + \langle\overline{u_i}\rangle \frac{\partial r_{ij}}{\partial x_j} = \langle\overline{u_i}\rangle \langle\overline{f_i}\rangle, \tag{8}$$

Rewriting Eq. (8) as a vector equation yields:

$$\nabla \cdot \{\langle\overline{E}\rangle \langle\overline{\mathbf{u}}\rangle + \langle\overline{\mathbf{T}}\rangle\} = -\Gamma + P_T, \tag{9}$$

where,

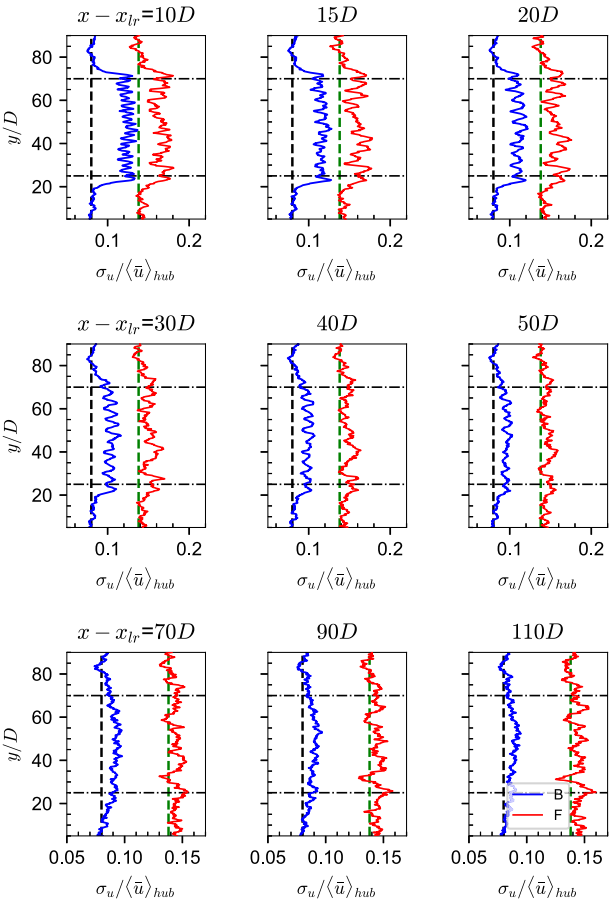

Fig. 15 Spanwise profiles of the time-averaged turbulence intensity at hub height for different downstream positions relative to the last-row wind turbines located at x_{lr}. The 'B' and 'F' in the legend represent WF B and F for $k_0 = 0.001$ m and 0.1 m, respectively. The vertical black (green) dashed line corresponds to $\sigma_u/\langle\bar{u}\rangle_{hub} = 0.080$ (0.138), which represents the inflow turbulence intensity of WF B (F). The black dotted-dash lines represent the spanwise boundaries of the wind farms

$$
\begin{aligned}
\langle\overline{E}\rangle &= \frac{1}{2}\langle\overline{u_i}\rangle\langle\overline{u_i}\rangle, \\
\left\langle\overline{T}_i\right\rangle &= \frac{\langle\bar{p}\rangle}{\rho}\langle\overline{u_i}\rangle + r_{ij}\left\langle\overline{u_j}\right\rangle, \\
\Gamma &= -r_{ij}\frac{\partial\langle\overline{u_i}\rangle}{\partial x_j}, \\
P_T &= \langle\overline{u_i}\rangle\left\langle\overline{f_i}\right\rangle.
\end{aligned}
\tag{10}
$$

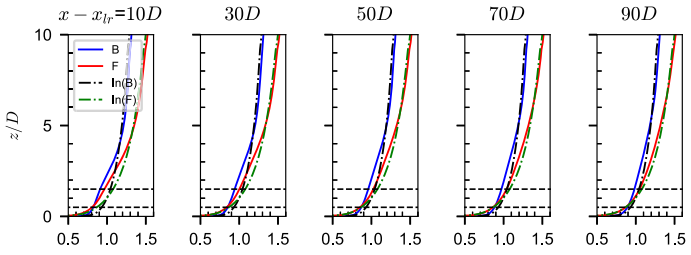

(a) Streamwise velocity $\langle \bar{u} \rangle / \langle \bar{u} \rangle_{hub}$

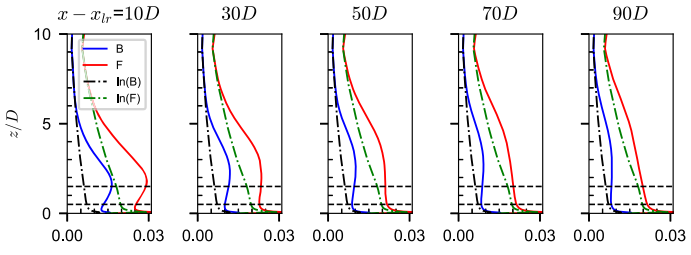

(b) Streamwise component of Reynolds stresses $\left\langle \overline{u'u'} \right\rangle / \langle \bar{u} \rangle_{hub}{}^2$

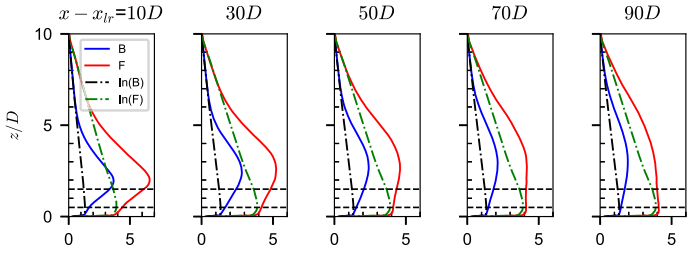

(c) Primary Reynolds shear stress $-\left\langle \overline{u'w'} \right\rangle / \langle \bar{u} \rangle_{hub}{}^2 \times 10^3$

Fig. 16 Vertical profiles of the time- and spanwise-averaged statistics at different downstream locations relative to the last row of the wind farm. The black dashed lines show the top and bottom tips of the wind turbine rotor. The 'B' and 'F' in the legend represent WF B and F for $k_0 = 0.001$ m and 0.1 m, respectively. The lines with 'In(B)' and 'In(F)' in legends show the statistics of the inflow of WF B and F

Selecting a control volume enclosing the wind farm and its wake region, the integral form the MKE budget equation is obtained in the following form,

$$\int_S \{\langle \overline{E} \rangle \langle \overline{\mathbf{u}} \rangle + \langle \overline{\mathbf{T}} \rangle\} \cdot d\mathbf{s} = \int_V -\Gamma dv + \int_V P_T dv, \tag{11}$$

which describes the balance between the energy fluxes and energy sinks for the MKE in the control volume. The energy fluxes at the control surface include the one caused by the mean flow, i.e., $\langle \bar{E} \rangle \langle \overline{\mathbf{u}} \rangle$, the one due to pressure transport, i.e., $\frac{\langle \bar{p} \rangle}{\rho} \langle \overline{u_i} \rangle$, and the one due to turbulence convection, i.e., $r_{ij} \langle \overline{u_j} \rangle$. The energy sink terms include Γ and P_T. The term Γ is the production term of the turbulence kinetic energy, and the term P_T is the rate of energy extraction by wind turbines.

For the energy fluxes in the streamwise direction, the terms $r_{12} \langle \overline{u_2} \rangle$ and $r_{13} \langle \overline{u_3} \rangle$ of small magnitude are neglected, resulting the examined streamwise energy flux in the following

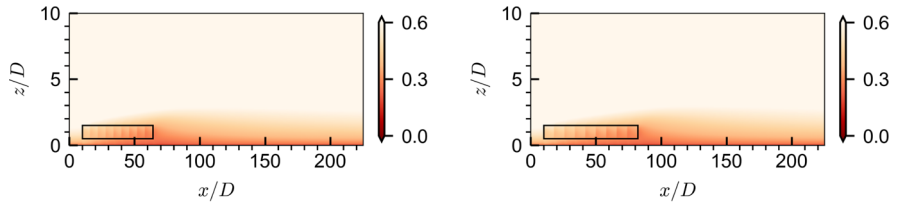

(a) WF A ($S_x = 6D, k_0 = 0.001, N_{row} = 10$) (b) WF B ($S_x = 8D, k_0 = 0.001, N_{row} = 10$)

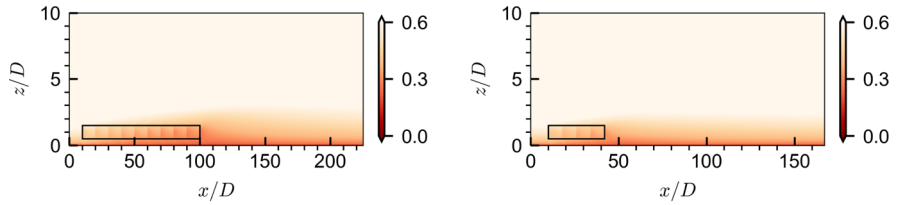

(c) WF C ($S_x = 10D, k_0 = 0.001, N_{row} = 10$) (d) WF D ($S_x = 8D, k_0 = 0.001, N_{row} = 5$)

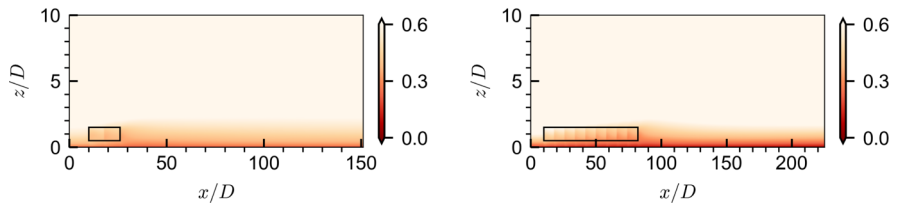

(e) WF E ($S_x = 8D, k_0 = 0.001, N_{row} = 3$) (f) WF F ($S_x = 8D, k_0 = 0.1, N_{row} = 10$)

Fig. 17 Contours of the streamwise energy flux, i.e., $\langle \overline{E} \rangle \langle \overline{u_1} \rangle + \frac{\langle \overline{p} \rangle}{\rho} \langle \overline{u_1} \rangle + r_{11} \langle \overline{u_1} \rangle$, which is normalized using $\langle \bar{u} \rangle_{hub}{}^3$ for **a** WF A, **b** WF B, **c** WF C, **d** WF D, **e** WF E and **f** WF F, respectively. The black solid line encloses the region with the wind farm. It is noted that the horizontal and vertical axes are not scaled in the same way

form,

$$\text{Flux}_1 = \int_{S_1} \left\{ \langle \overline{E} \rangle \langle \overline{u_1} \rangle + \frac{\langle \overline{p} \rangle}{\rho} \langle \overline{u_1} \rangle + r_{11} \langle \overline{u_1} \rangle \right\} \cdot ds_1. \tag{12}$$

For the vertical component, the two dominant terms are the mean convection term and the turbulence convection term, which are expressed as follows:

$$\text{Flux}_3 = \int_{S_3} \left\{ \langle \overline{E} \rangle \langle \overline{u_3} \rangle + r_{13} \langle \overline{u_1} \rangle \right\} \cdot d\mathbf{s}_3. \tag{13}$$

The streamwise energy flux is firstly examined in Fig. 17. It is seen that the overall magnitude of the energy flux is the greatest in the region near the downstream end of the wind farm. The vertical extent of the region with significant streamwise energy flux is greater within the wind farm and in its wake when compared with the inflow. As the streamwise pressure convection $\frac{\langle \overline{p} \rangle}{\rho} \langle \overline{u_1} \rangle$ and streamwise turbulent convection $r_{11} \langle \overline{u_1} \rangle$ in Eq. (12) are much smaller in magnitude than the streamwise mean convection $\langle \overline{E} \rangle \langle \overline{u_1} \rangle$ (the analysis is

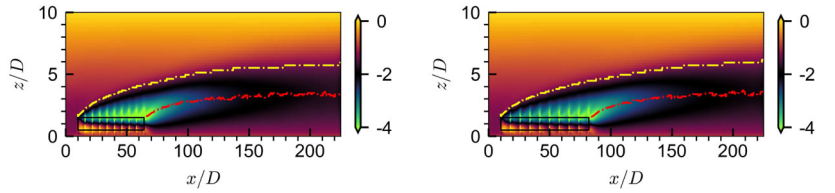

(a) WF A ($S_x = 6D, k_0 = 0.001, N_{row} = 10$) (b) WF B ($S_x = 8D, k_0 = 0.001, N_{row} = 10$)

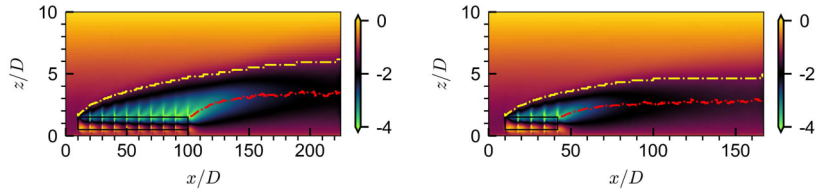

(c) WF C ($S_x = 10D, k_0 = 0.001, N_{row} = 10$) (d) WF D ($S_x = 8D, k_0 = 0.001, N_{row} = 5$)

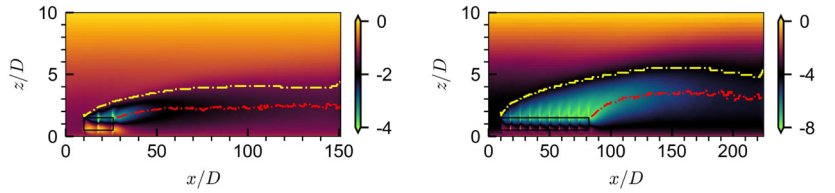

(e) WF E ($S_x = 8D, k_0 = 0.001, N_{row} = 3$) (f) WF F ($S_x = 8D, k_0 = 0.1, N_{row} = 10$)

Fig. 18 Contours of the vertical MKE flux due to turbulence convection, i.e., the term $r_{13}\langle\overline{u_1}\rangle$, which is multiplied by a factor of 1000 and normalized with $\langle\bar{u}\rangle_{hub}{}^3$. The yellow dash-dotted line with $r_{13}\langle\overline{u_1}\rangle = r_{13}\langle\overline{u_1}\rangle_{in}$ ($r_{13}\langle\overline{u_1}\rangle_{in}$ is the value of $r_{13}\langle\overline{u_1}\rangle$ at $1D$ upstream of the first row of turbines at the top-tip) is employed to indicate the upper boundary of the region with strong turbulence convection. The red dash-dotted line shows the location with the maximum magnitude of $r_{13}\langle\overline{u_1}\rangle$ at each downstream location from the downstream end of the wind farm. The black solid line encloses the region with the wind farm. It is noted that the horizontal and vertical axes are not scaled in the same way

not shown in the paper), the contributions from different terms in the streamwise energy flux are not examined individually.

The momentum mixing of wakes in the horizontal plane will achieve an equilibrium state as one travels in the wind farm downstream direction, that the only source for energy replenishment of the wake is from its upper region. The vertical MKE flux due to turbulence mixing, i.e., $r_{13}\langle\overline{u_1}\rangle$, which is well known being the key mechanism (Stevens and Meneveau 2017; Porté-Agel et al. 2020), is firstly examined in Fig. 18. It is seen that the term $r_{13}\langle\overline{u_1}\rangle$ is of high magnitude in the region above the farm. In the wake of the farm, the vertical extent of the region with high magnitude of $r_{13}\langle\overline{u_1}\rangle$ increases, with the vertical location with the maximum magnitude of $r_{13}\langle\overline{u_1}\rangle$ moving upward, and achieves a plateau in the wind farm's far wake ($x - x_{lr} > 90D$) region. Similar trends are observed for the three wind farms with different streamwise turbine spacings. Higher magnitude of vertical MKE flux due to turbulence convection is observed in Fig. 18f for the case with a higher roughness length of ground surface.

Gadde and Stevens (2021), Kadum et al. (2020) and Allaerts and Meyers (2017) performed MKE budget analysis for each row of wind turbines in a wind farm, showing that the mean

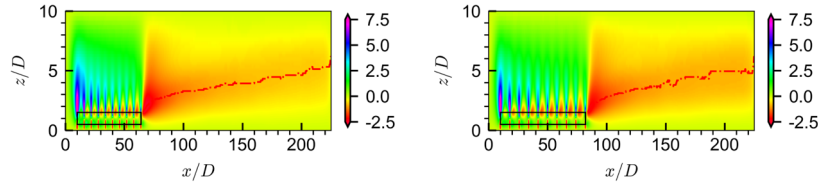

(a) WF A ($S_x = 6D, k_0 = 0.001, N_{row} = 10$) (b) WF B ($S_x = 8D, k_0 = 0.001, N_{row} = 10$)

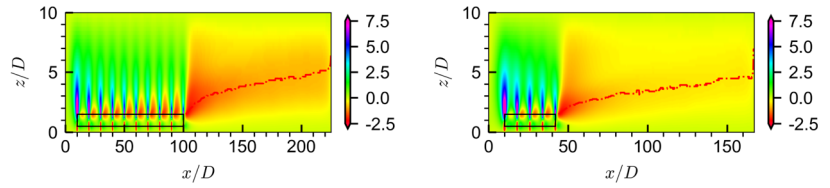

(c) WF C ($S_x = 10D, k_0 = 0.001, N_{row} = 10$) (d) WF D ($S_x = 8D, k_0 = 0.001, N_{row} = 5$)

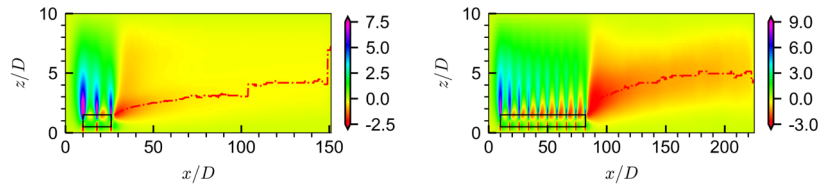

(e) WF E ($S_x = 8D, k_0 = 0.001, N_{row} = 3$) (f) WF F ($S_x = 8D, k_0 = 0.1, N_{row} = 10$)

Fig. 19 Vertical MKE flux due to mean convection, i.e. the term $\langle \overline{E} \rangle \langle \overline{u_3} \rangle$, which is multiplied by a factor of 1000 and normalized with $\langle \bar{u} \rangle_{hub}{}^3$. The red dash-dotted line shows the location with the maximum magnitude of $\langle \overline{E} \rangle \langle \overline{u_3} \rangle$ at each downstream location from the downstream end of the wind farm. In (e), WF E is not good at capturing the maximum magnitude because the wake is almost restored ($x > 120D$). The black solid line encloses the region with the wind farm. It is noted that the horizontal and vertical axes are not scaled in the same way

convection promotes wake recovery, but without the analysis of the contribution in each direction. In this work, we specifically examine the contribution in the vertical direction in Fig. 19, which plays a role on the MKE transport as indicated by the distribution of the vertical velocity shown in Fig. 5.

It is seen that the term $\langle \overline{E} \rangle \langle \overline{u_3} \rangle$ is featured by positive (upward) and negative (downward) regions around the top tip region in the farm. Similar results were shown in the simulations by Stieren and Stevens (2022) and Maas (2022). In the wake of the wind farm wake area, on the other hand, a significant amount of MKE is transported downwards from the upper region of wake via mean convection, and which is consistent with the observation by Rolin and Porté-Agel (2018). And the vertical extent of the region with significant mean convection increases as the flow develops in the downstream direction.

Figure 20 further examines the streamwise variations of the vertical locations of the maximum turbulence convection (i.e., $r_{13} \langle \overline{u_1} \rangle$), the maximum mean convection (i.e., $\langle \overline{E} \rangle \langle \overline{u_3} \rangle$) and the upper boundary of the region with significant turbulence convection (in which the upper boundary is defined as the location of $r_{13} \langle \overline{u_1} \rangle = r_{13} \langle \overline{u_1} \rangle_{in}$, where $r_{13} \langle \overline{u_1} \rangle_{in}$ is taken at 1D upstream of the first row and at the height of rotor's top tip). It is seen that the vertical extent of the region with significant turbulence convection is larger for cases with larger

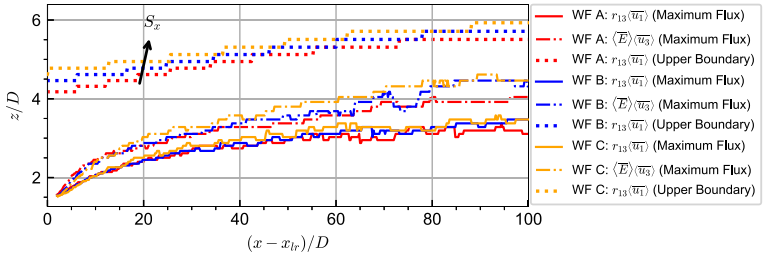

(a) WF A, B and C: different turbines spacings

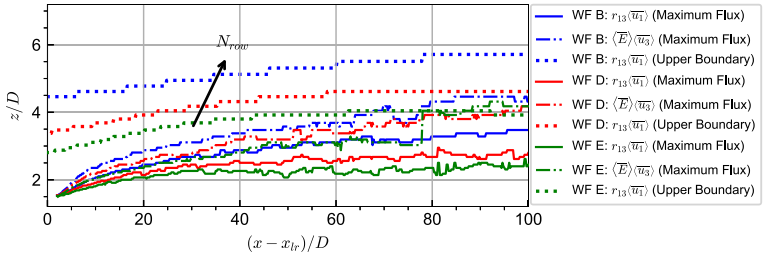

(b) WF B, D and E: different turbines rows

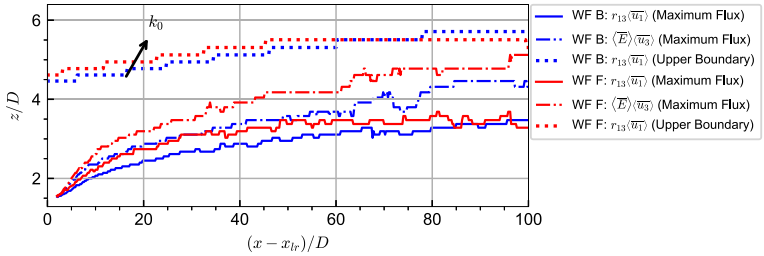

(c) WF B and F: different roughness lengths of ground surface

Fig. 20 Vertical locations of the maximum vertical MKE flux due to turbulence convection ($r_{13}\,\langle\overline{u_1}\rangle$, solid lines) and mean convection ($\langle\overline{E}\rangle\,\langle\overline{u_3}\rangle$, dash-dotted lines), and the upper boundary of the region with significant turbulence convection (dotted lines). Arrows with annotations in **a**, **b** and **c** indicate the direction of increase in streamwise turbine spacings, number of rows and roughness lengths of ground surface, respectively

streamwise turbine spacing, more rows of wind turbines and higher roughness length of ground surface. The maximum MKE flux due to mean convection is also in general observed at a higher vertical location for cases with larger streamwise turbine spacing, more turbines rows and larger roughness length of ground surface, with uncertainty in wind farm's far wake ($x - x_{lr} > 90D$) locations probably due to the uncertainty in identifying the maximums. The vertical locations for the maximum MKE flux due to turbulence convection, on the other hand, are fairly close to each other for different streamwise turbine spacing. Figure 21 shows the streamwise variations of $r_{13}\,\langle\overline{u_1}\rangle$ and $\langle\overline{E}\rangle\,\langle\overline{u_3}\rangle$ with the maximum magnitudes. It is seen that their magnitudes decrease as the flow develops in the downstream direction, with those of $\langle\overline{E}\rangle\,\langle\overline{u_3}\rangle$ being smaller. For cases with different streamwise turbine spacings (S_x), the magnitudes of both terms are larger for smaller S_x in the wind farm's near wake (which

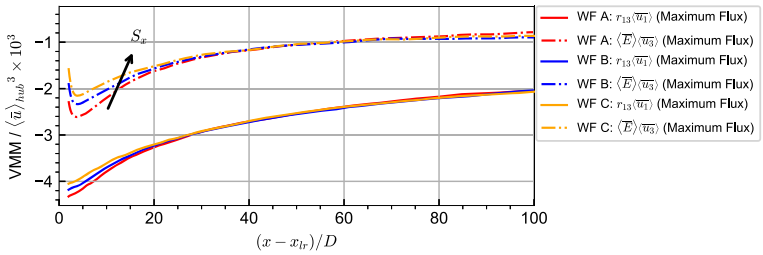

(a) WF A, B and C: different turbines spacings

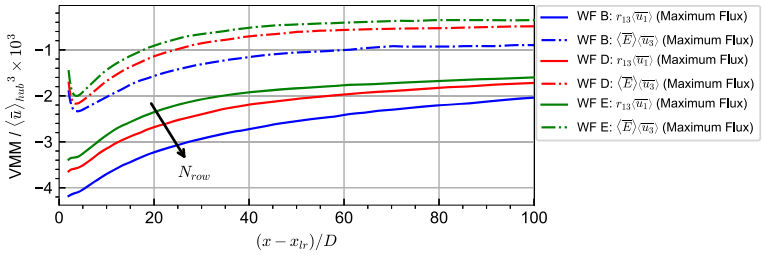

(b) WF B, D and E: different turbines rows

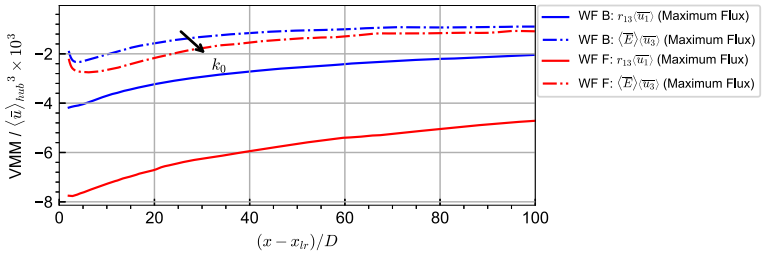

(c) WF B and F: different roughness lengths of ground surface

Fig. 21 Values of $r_{13}\,\langle\overline{u_1}\rangle$ (solid lines) and $\langle\overline{E}\rangle\,\langle\overline{u_3}\rangle$ (dash-dotted lines) with the maximum magnitude (VMM), which were multiplied by a factor of 1000 and normalized with $\langle\bar{u}\rangle_{hub}{}^3$. Arrows with annotations in **a**, **b** and **c** indicate the direction of increase in streamwise turbine spacings, number of rows and roughness lengths of ground surface, respectively

is defined as $x - x_{lr} < 20D$), as shown in Fig. 21a. For more rows of wind turbines and higher roughness length, both magnitudes are larger, with more significant differences in the turbulent convection term $r_{13}\,\langle\overline{u_1}\rangle$, as shown in Fig. 21b, c.

To further quantitatively examine the downstream variations of the vertical MKE flux, Fig. 22 shows the differences of the vertical MKE flux between the top and bottom tips of the wind farm in the vertical direction (net vertical MKE flux), i.e., $\left\langle\overline{u'w'}\right\rangle\,\langle\overline{u}\rangle\,|_{z=bottom}^{z=top}$ and $\langle\overline{E}\rangle\,\langle\overline{w}\rangle\,|_{z=bottom}^{z=top}$ for turbulence convection and mean convection, respectively. It is seen that the net vertical MKE fluxes are larger in the wind farm's near wake ($x - x_{lr} < 20D$) region for cases with smaller streamwise spacing and more rows of wind turbines, while they are similar with each other in the wind farm's far wake ($x - x_{lr} > 90D$) region, as shown in Fig. 22a, b. Figure 22c shows that the net vertical MKE fluxes due to turbulence are larger for higher roughness length. The net vertical MKE fluxes due to mean convection and turbulence convection are found being of the same order, with the latter one being larger.

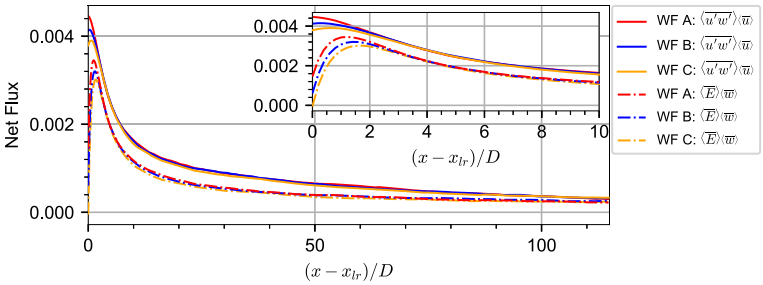

(a) WF A, B and C: different turbines spacings

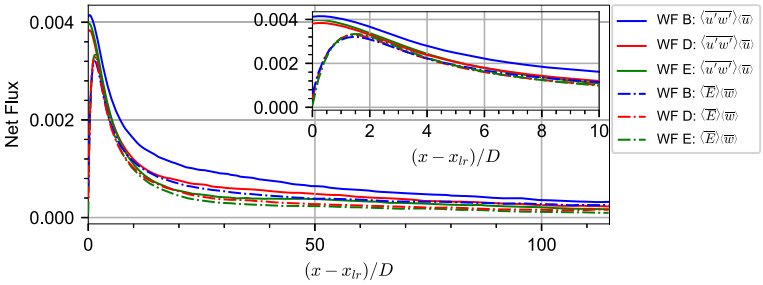

(b) WF B, D and E: different turbines rows

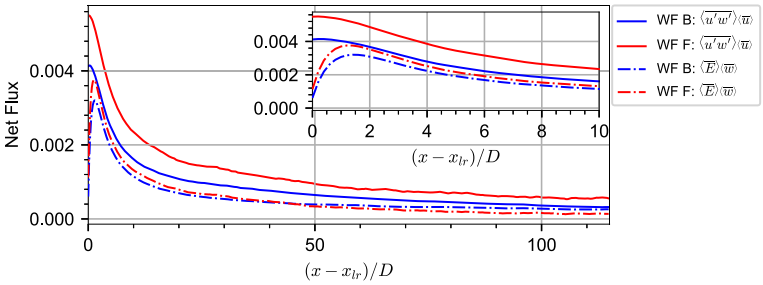

(c) WF B and F: different roughness lengths of ground surface

Fig. 22 Net vertical MKE fluxes in wind farm wake region due to turbulence convection (solid lines) and mean convection (dash-dotted lines). The net flux is computed as the difference between the values of corresponding terms at the top and bottom tips of the wind farm, i.e., $\left\langle \overline{u'w'} \right\rangle \langle \overline{u} \rangle \,|_{z_{hub}-0.5D}^{z_{hub}+0.5D} / \langle \bar{u} \rangle_{hub}{}^3$, $\langle \overline{E} \rangle \langle \overline{w} \rangle \,|_{z_{hub}-0.5D}^{z_{hub}+0.5D} / \langle \bar{u} \rangle_{hub}{}^3$

To further examine the effects of different vertical MKE flux terms and the balance with the streamwise MKE flux, a control volume is employed to integrate Eqs. 12 and 13 as follows:

$$\mathcal{FLUX}_3 = \int_{x=upstream}^{x=downstream} \left\{ \langle \overline{E} \rangle \langle \overline{w} \rangle + \left\langle \overline{u'w'} \right\rangle \langle \overline{u} \rangle \right\} \cdot d\mathbf{s_3} \,|_{z=bottom}^{z=top},$$

$$\mathcal{F}_{3\mathcal{E}} = \int_{x=upstream}^{x=downstream} \left\{ \langle \overline{E} \rangle \langle \overline{w} \rangle \right\} \cdot d\mathbf{s_3} \,|_{z=bottom}^{z=top},$$

$$\mathcal{F}_{3\mathcal{T}} = \int_{x=upstream}^{x=downstream} \left\{ \left\langle \overline{u'w'} \right\rangle \langle \overline{u} \rangle \right\} \cdot d\mathbf{s_3} \,|_{z=bottom}^{z=top},$$

$$
\begin{aligned}
\mathcal{FLUX}_I &= \int_{z=bottom}^{z=top} \left\{ \langle \overline{E} \rangle \langle \overline{u} \rangle + \frac{\langle \overline{p} \rangle}{\rho} \langle \overline{u} \rangle + \left\langle \overline{u'u'} \right\rangle \langle \overline{u} \rangle \right\} \cdot d\mathbf{s_1} \,|_{x=upstream}^{x=downstream}, \\
\mathcal{F}_{I\mathcal{E}} &= \int_{z=bottom}^{z=top} \left\{ \langle \overline{E} \rangle \langle \overline{u} \rangle \right\} \cdot d\mathbf{s_1} \,|_{x=upstream}^{x=downstream}, \\
\mathcal{F}_{I\mathcal{P}} &= \int_{z=bottom}^{z=top} \left\{ \frac{\langle \overline{p} \rangle}{\rho} \langle \overline{u} \rangle \right\} \cdot d\mathbf{s_1} \,|_{x=upstream}^{x=downstream}, \\
\mathcal{F}_{I\mathcal{T}} &= \int_{z=bottom}^{z=top} \left\{ \left\langle \overline{u'u'} \right\rangle \langle \overline{u} \rangle \right\} \cdot d\mathbf{s_1} \,|_{x=upstream}^{x=downstream}, \\
\mathcal{P}_{\mathcal{TKE}} &= \int_{z=bottom}^{z=top} \int_{x=upstream}^{x=downstream} \left\{ r_{ij} \frac{\partial \langle \overline{u_i} \rangle}{\partial x_j} \right\} dx dz, \\
\mathcal{P}_{\mathcal{T}} &= \int_{z=bottom}^{z=top} \int_{x=upstream}^{x=downstream} \left\{ \langle \overline{u_i} \rangle \left\langle \overline{f_i} \right\rangle \right\} dx dz,
\end{aligned} \tag{14}
$$

where three integral domains are selected for analysis, as shown in Fig. 23. In Fig. 23a, b, the control volume is selected as the wind farm region with $x_{upstream} = x_{fr} - 1D$ and $x_{downstream} = x_{lr} + 1D$, and $x_{upstream} = x_{sr} - 1D$ and $x_{downstream} = x_{lr} + 1D$, respectively. In Fig. 23c, the control volume is selected as the wake region of the wind farm with $x_{upstream} = x_{lr} + 5D$ and $x_{downstream} = x_{lr} + 115D$. The integral range is from $z_{bottom} = z_{hub} - 0.5D$ to $z_{top} = z_{hub} + 0.5D$ in the vertical direction, and from the first column $y_{fc} - 0.5D$ to the last column $y_{lc} + 0.5D$ (where y_{fc} and y_{lc} denote the spanwise coordinate of the rotor center for the first column and the last column) of the wind turbines in the spanwise direction, respectively.

Figure 23 shows several term in Eq. (14), with positive and negative values indicating MKE flux flowing into and out the control volume, respectively. The residual term, $\mathcal{R} = \int_{S_x} \{\langle \overline{u}''\overline{u}'' \rangle \langle \overline{u} \rangle + r_{12} \langle \overline{v} \rangle + r_{13} \langle \overline{w} \rangle\} \, ds_x + \int_{S_y} \{\langle \overline{E} \rangle \langle \overline{v} \rangle + \langle \overline{T}_2 \rangle\} \, ds_y + \int_{S_z} \{\frac{\langle \overline{p} \rangle}{\rho} \langle \overline{w} \rangle + r_{32} \langle \overline{v} \rangle + r_{33} \langle \overline{w} \rangle + \langle \overline{u}''\overline{w}'' \rangle \langle \overline{u} \rangle\} \, ds_z$, which includes the rest terms in the MKE budget equation, is also shown in Fig. 23. Figure 23a, b show the results when the wind farm is enclosed by the control volume. It is seen that the vertical turbulence convection and the streamwise mean convection are the two dominant factors for the recovery of velocity in wind farms except WF E, which is only dominated by streamwise mean convection. Because turbulent convection began to play a role after the third row of turbines (Maas 2022; Gadde and Stevens 2021). When changing the starting location of the control volume from the first row ($x_{upstream} = x_{fr} - 1D$) to the second row ($x_{upstream} = x_{sr} - 1D$), the streamwise MKE flux due to mean convection reduces by approximately 30%, indicating its significant role for turbines in the first row. And, the streamwise MKE flux caused by the pressure gradient is also reduced when the first row of wind turbines are not included in the control volume. One special attention is on the MKE flux due to mean convection, which leads to small MKE outflows from the wind farm region, consistent with Maas (2022). Then, the contributions of different MKE flux terms in the wind farm wake are examined in Fig. 23c. First, it is seen that the magnitudes of $\mathcal{FLUX}_3$ and $\mathcal{FLUX}_I$ are close to each other, that they are the two terms dominates the MKE budget in wind farm's wake. The difference between the two terms increases as the roughness length of the ground surface increases (i.e., WF B vs. WF F). By comparing the magnitudes of $\mathcal{FLUX}_3$ and $\mathcal{FLUX}_I$ from cases with different streamwise turbine spacing, it is observed that they decreases with the increase of streamwise turbine spacing at a low rate. Different from the wind farm region, the vertical MKE flux due to mean convection together with that due to turbulence convection now serve as the key mechanisms for velocity recovery. The streamwise MKE flux, which dominates the loss of MKE in the control volume, is found

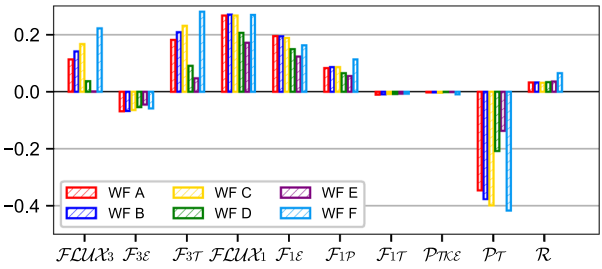

(a) $x_{upstream} = x_{fr} - 1D$, and $x_{downstream} = x_{lr} + 1D$

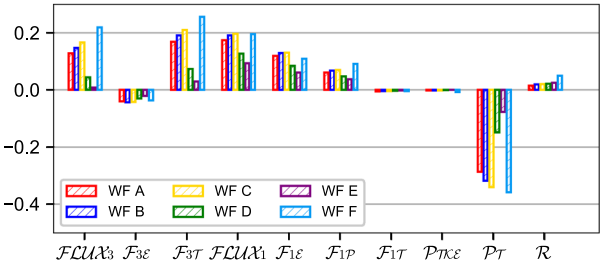

(b) $x_{upstream} = x_{sr} - 1D$, and $x_{downstream} = x_{lr} + 1D$

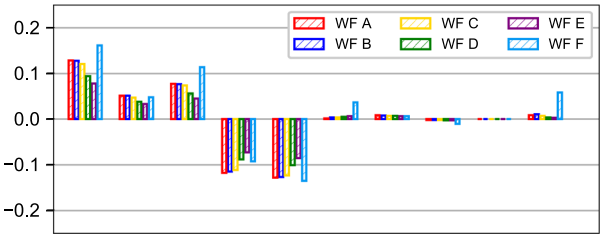

(c) $x_{upstream} = x_{lr} + 5D$, $x_{downstream} = x_{upstream} + 115D$

Fig. 23 Contributions of different terms in MKE budget (Eq. 14) for different control volumes: **a**, **b** wind farm; (c) wake of wind farm. Different terms are normalized using $\langle \bar{u} \rangle_{hub}{}^3 D^2$. The x_{fr} and x_{sr} represent the streamwise coordinates of the first and the second rows of wind turbines

being controlled by the mean convection with the magnitudes of the MKE fluxes due to turbulence convection and pressure transport being one order of magnitude smaller. That it is not close to machine zero is mainly due to the assumptions made in deriving the MKE budget equation (Eq. (8)). The relatively large magnitude of $\mathcal{R}$ for WF F is caused by the relatively high turbulence convection in the spanwise direction as indicated by the term $r_{i2} \langle \overline{v} \rangle$ shown in Fig. 14, and the relatively large magnitude of the dispersive terms (which have been examined but not shown in the paper), i.e., $\langle \overline{u}'' \overline{u}'' \rangle \langle \overline{u} \rangle$ and $\langle \overline{u}'' \overline{w}'' \rangle \langle \overline{u} \rangle$, which contribute to the $\mathcal{R}$ term.

4.3 Analytical Models for Wind Farm Wake

4.3.1 The Emeis Model

The analytical model proposed by Emeis (2010) is briefly described. In the Emeis model, the velocity in a wind farm's wake is computed using the following expression,

$$\frac{\partial U_w}{\partial t} = \frac{\partial(\tau/\rho)}{\partial z}, \tag{15}$$

where U_w is the velocity in wake at hub height, τ/ρ the vertical momentum flux with ρ the air density. The term τ/ρ is computed as follows,

$$\frac{\tau}{\rho} = K\frac{U_f - U_w}{\Delta z_f}, \tag{16}$$

where K is the momentum exchange coefficient, U_f is the freestream velocity, and Δz_f is the distance between the height where the flow is unaffected by the wind turbine and the hub height (Emeis 2010; Platis et al. 2021), which is typically measured at a downstream location (often 1 km) of the wind farm. Emeis considered $K = \kappa u_* z_f$, with $z_f = z_{hub} + \Delta z_f$, $\kappa = 0.4$ and u_* the friction velocity of the ground. With Eq. (16) and Eq. (15), the model for the velocity deficit $\Delta U_w(t)$ at hub height is obtained as follows in the original form of Emeis (2010):

$$\frac{\Delta U_w(t)}{U_f} = \frac{U_f - U_w(t)}{U_f} = \left(1 - \frac{U_{w,0}}{U_f}\right) e^{-\alpha t}, \tag{17}$$

where the wake recovery rate $\alpha = \kappa u_* \frac{z_f}{\Delta z_f{}^2}$, and the wake initial velocity $U_{w,0} = U_w(t = 0)$. With α, $U_{w,0}$ and U_f from measurements, the wake velocity deficit at hub height can then be calculated using Eq. (17).

In this work, we further derive Eq. (17) to express it as a function of the downstream location of the wind turbine. To compute the wake recovery rate, the friction velocity is obtained using the incoming velocity at hub height: $\frac{u_*}{\langle\bar{u}\rangle_{hub}} = \frac{k}{\ln(z_h/k_0)}$. The corresponding time is given by $t = \frac{x - x_m}{\langle\bar{u}\rangle_{hub}}$, where x_m is the position of the streamwise direction where the measurement point is located. Equation (17) is then expressed in the following form:

$$\frac{\Delta U_w(x)}{U_f} = \frac{\Delta U_{w,0}}{U_f} \cdot \exp\left(-\beta\frac{x - x_m}{D}\right), \tag{18}$$

where $\Delta U_{w,0} = U_f - U_{w,0}$ is the velocity deficit at the measurement point position, and $\beta = \frac{\kappa^2}{\ln(z_h/k_0)} \frac{z_f/D}{(\Delta z_f/D)^2}$ is the wake recovery factor.

When employing the Emeis model for the simulated cases, the velocity at the measurement point x_m, which is located 1 km downstream of the wind farm, is obtained from the LES results. The U_f is set as $\langle\bar{u}\rangle_{hub}$.

4.3.2 The Modified Emeis Model

The Emeis model is further modified to include the effect of vertical mean convection and better account for the effect of ground roughness.

The key modification is in how the vertical momentum flux τ/ρ is modeled. Considering that it is related to the Reynolds shear stress and the vertical mean convection, as shown by the LES results, and that it must reduce to zero when the streamwise velocity fully recovers, the model for τ/ρ is proposed in the following form,

$$\tau U_w/\rho = -\overline{u'w'}\,(U_{hub} - U_w) - {U_w}^2 W_w, \tag{19}$$

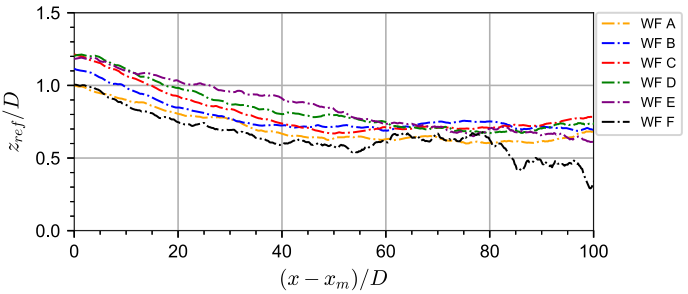

Fig. 24 Reference height z_{ref} for computing K_m for the simulated six wind farms

where $\langle \bar{u} \rangle_{hub}$ is expressed as U_{hub} for simplicity, and W_w is the vertical velocity. In the above equation, $\tau(x)/\rho$ is modeled as,

$$\frac{\tau_m}{\rho} = K_m \frac{U_{hub} - U_w}{D}, \tag{20}$$

which is zero as U_w recovers to U_{hub}. The expression for K_m is given as follows,

$$K_m = \kappa u_* z_{ref}. \tag{21}$$

Different from the Emeis model, in which $z_{ref} = z_f$, in the modified Emeis model z_{ref} is determined by substituting Eqs. (20) and (21) in to Eq. (19) with the right-hand-side of Eq. 19 given by the LES results at hub height.

With the value of z_{ref} to be determined using the LES results, the modified Emeis model is expressed as follows:

$$\frac{\Delta U_w(x)}{U_{hub}} = \frac{\Delta U_{w,0}}{U_{hub}} \cdot \exp\left(-\beta_m \frac{x - x_m}{D}\right), \tag{22}$$

where $\beta_m = \frac{\kappa^2}{\ln(z_h/k_0)} \frac{z_{ref}}{D}$

The values of z_{ref} obtained are shown in Fig. 24. It is seen that reference height z_{ref} of the six wind farms are very close, with small variations in the streamwise direction. For simplicity, the mean value of z_{ref} averaged in the streamwise direction and over different cases is employed, which is $z_{ref} = 0.77D$.

There are two key factors affecting the model performance, i.e., the way in modeling the momentum exchange coefficient (K or K_m) and the way in approximating the velocity gradient in Eqs. (16) or (20). For the former factor, it is about the reference height z_{ref} employed for computing K or K_m. In the Emeis model, z_{ref} is taken as the height (z_f) where the streamwise velocity recovers to the freestream velocity. Such approach needs measurements at various vertical locations. Furthermore, z_f is not necessarily the location where most momentum mixing happens. In the modified Emeis model proposed in this paper, the reference height z_{ref} is assumed being close to a constant for most wind farm downstream locations, which is approximately valid as shown in Fig. 24. For the latter factor, the term $(U_f - U_w)/\Delta z_f$ in Eq. (16) of the Emeis model does not decrease to zero when U_w recovers to U_{hub}, as U_f taken at the measurement point z_f is different from U_{hub}. This causes a problem that U_w asympototes to U_f instead of U_{hub}. To avoid this issue, the modified Emeis model approximates the velocity gradient using a characteristic velocity difference and a characteristic length scale, which are $U_{hub} - U_w$ and D, respectively. Overall, the modified Emeis model avoids the need of measurements at various vertical positions (while it still

Table 2 Mean relative errors of the Emeis ($\langle e_r \rangle_{\mathrm{E}}$) models

Case	$\frac{\langle \Delta U_{w,0} \rangle}{\langle \bar{u} \rangle_{hub}}$	z_f	Δz_f	k_0(m)	β	$\langle e_r \rangle_{\mathrm{E}}$ (%)
WF A	0.13149	3.6D	2.6D	0.001	0.0074	28.5
WF B	0.13121	3.8D	2.8D	0.001	0.0067	31.9
WF C	0.12740	4.0D	3.0D	0.001	0.0062	34.9
WF D	0.09127	3.4D	2.4D	0.001	0.0082	28.2
WF E	0.06904	3.1D	2.1D	0.001	0.0098	26.0
WF F	0.09553	4.1D	3.1D	0.1	0.0099	115.3

Table 3 Mean relative errors of the modified Emeis ($\langle e_r \rangle_{\mathrm{mE}}$) models

Case	$\frac{\langle \Delta U_{w,0} \rangle}{\langle \bar{u} \rangle_{hub}}$	z_{ref}	k_0(m)	β_m	$\langle e_r \rangle_{\mathrm{mE}}$ (%)
WF A	0.13149	0.77D	0.001	0.0107	7.7
WF B	0.13121	0.77D	0.001	0.0107	6.7
WF C	0.12740	0.77D	0.001	0.0107	6.1
WF D	0.09127	0.77D	0.001	0.0107	12.2
WF E	0.06904	0.77D	0.001	0.0107	19.9
WF F	0.09553	0.77D	0.1	0.0178	33.4

needs the velocity deficit at hub height at one wind farm downstream position), and satisfies the asymptotic requirement at the fully-recovered wake state.

4.3.3 Results of the Analytical Models

The predictions of the Emeis model and the modified Emeis model are presented in this subsection.

To quantitatively evaluate the predictive ability of the models, the mean relative error ($\langle e_r \rangle$) is examined, which is defined as,

$$e_r(x) = \frac{\left| \Delta U_w^M(x) - \Delta U_w^{LES}(x) \right|}{\Delta U_w^{LES}(x)}. \tag{23}$$

The averaging for obtaining the mean of e_r is carried out from x_m to $x_{lr} + 115D$.

The mean relative errors and the coefficients of the Emeis model (Eq. (18)) are shown in Table 2. Errors greater than 25% are observed. It is also noted that the error exceeds 100% for case F. In the test of the modified Emeis model, the same measurement point is employed. The mean relative errors and the coefficients of the modified Emeis model (Eq. (22)) are shown in Table 3. The reduction of the mean relative errors is more than 10% (expect for case E, which is 7%).

Figure 25 shows the comparison of the velocity deficit predicted by the analytical models with the LES results. It is seen that the Emeis model underpredicts the velocity recovery. As for the modified Emeis model, improvements are observed for all the simulated cases.

The dependence of the prediction ability of the modified Emeis model on the selection of the measurement point x_m is examined in Fig. 26. It is seen that the further the measurement point, the higher the prediction accuracy of the model.

Overall, an acceptable agreement is observed for the modified Emeis model. One inherent limitation of this type of analytical model, which essentially describes how the velocity deficit

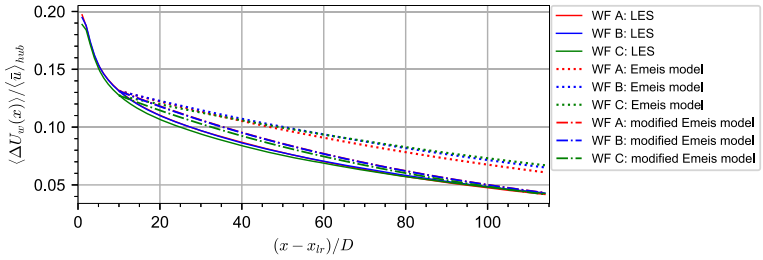

(a) WF A, B and C: different turbines spacings

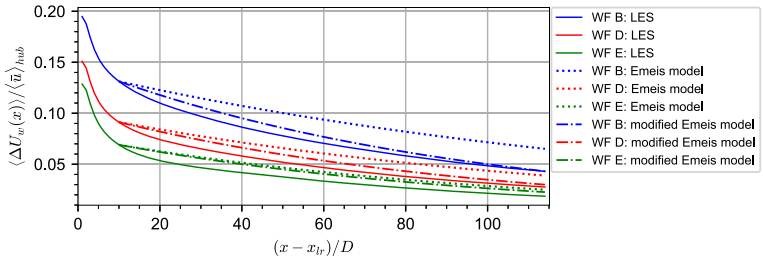

(b) WF B, D and E: different turbines rows

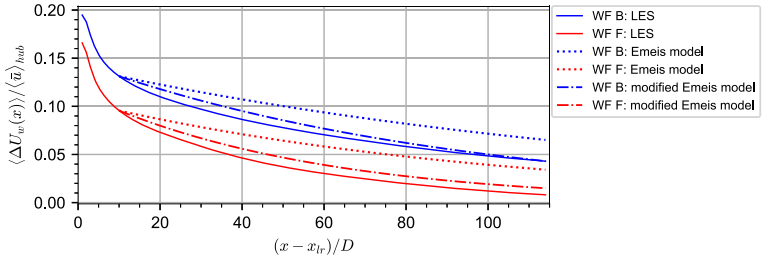

(c) WF B and F: different roughness lengths of ground surface

Fig. 25 Spanwise-averaged velocity deficit at hub height in the wind farm wake, in which solid lines, dotted lines and dash-dotted lines represent the results from LES, the Emeis model and the modified Emeis model, respectively

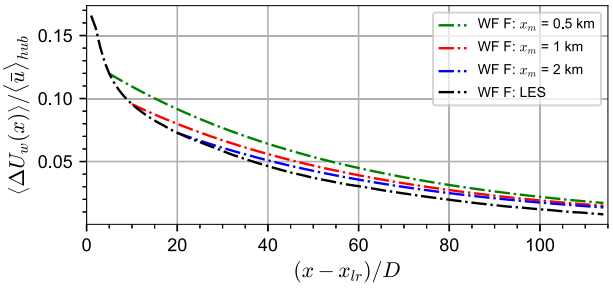

Fig. 26 Spanwise-averaged velocity deficit at hub height in the wind farm wake for WF F, in which solid line represents the result from LES, and dash-dotted lines represent the results from the modified Emeis model for three measurement points (i.e., $x_m = 0.5$ km,1 km and 2 km downstream of the wind farm). The mean relative errors are 50.9%, 33.5% and 24.3% for $x_m = 0.5$ km,1 km and 2 km, respectively

decays, is that it requires the velocity deficit at a specific downstream location of the wind farm, which may not be available in real-life applications.

5 Conclusions

In this work, we simulates wind farm wakes for different streamwise wind turbine spacings (i.e., $S_x = 6D$, $8D$ and $10D$), number of rows of wind turbines (i.e., $N_{row} = 10$, 5 and 3) and ground surface roughness lengths (i.e., $k_0 = 0.001$ m and 0.1m). For the wind farm with $S_x = 8D$, we carries out one additional case with a higher roughness length (i.e., $k_0 = 0.1$ m), and two additional cases with fewer rows of wind turbines ($N_{row} = 3$, 5).

Effects of streamwise turbine spacing on wake statistics are observed in the wind farm's near wake ($(x - x_{lr}) < 20D$, where x_{lr} denotes the streamwise coordinate of the last row), where the turbulence intensity σ_u is higher for the cases with smaller streamwsie turbine spacings. In wind farm's far wake, the velocity deficit and Reynolds stresses from cases with different values of S_x are close to each other. The effects of number of rows of wind turbines and roughness length of ground surface, on the other hand, are evident in both the near and far wake of the wind farm, where higher magnitudes of turbulence intensity σ_u and Reynolds shear stress $-\left\langle \overline{u'w'} \right\rangle$ are observed for cases with more rows of turbines (N_{row}) and higher roughness length of ground surface (k_0).

The budget equation for mean kinetic energy (MKE) is then analyzed. It is observed that the vertical MKE transport for the velocity recovery in a wind farm's wake is dominated by both turbulence convection and mean convection, with more contribution from the former one. For a control volume located in the wake, the streamwise MKE flux due to mean convection is the dominant term for the loss of MKE. The wake-influenced region in the vertical direction, in terms of high magnitude of turbulence convection, is observed to be larger for cases with larger values of S_x (i.e., a increase of $\sim$ 50 m in the height of wake-influenced region for a increase of $2D$ in S_x), larger numbers of rows of wind turbines, and higher roughness lengths of ground surface.

At last, an analytical model (the modified Emeis model) for predicting the streamwise variation of the velocity deficit is proposed based the Emeis model to take into account the effect of vertical mean convection. Improvements are observed for all the simulated cases for the modified Emeis model. On major limitation of the analytical model of this type is that the velocity deficit at one downstream location of the wind farm is required, and the corresponding location affects the prediction accuracy of the model.

Acknowledgements This work was supported by NSFC Basic Science Center Program for "Multiscale Problems in Nonlinear Mechanics" (No. 11988102), National Natural Science Foundation of China (No. 12172360), Institute of Mechanics CAS, and Chinese Academy of Sciences.

References

Ali N, Hamilton N, Calaf M, Cal RB (2019) Turbulence kinetic energy budget and conditional sampling of momentum, scalar, and intermittency fluxes in thermally stratified wind farms. J Turbul 20(1):32–63

Allaerts D, Meyers J (2017) Boundary-layer development and gravity waves in conventionally neutral wind farms. J Fluid Mech 814:95–130

Allaerts D, Meyers J (2018) Gravity waves and wind-farm efficiency in neutral and stable conditions. Boundary-Layer Meteorol 166(2):269–299

Allaerts D, Meyers J (2019) Sensitivity and feedback of wind-farm-induced gravity waves. J Fluid Mech 862:990–1028
Bossuyt J, Meneveau C, Meyers J (2018) Effect of layout on asymptotic boundary layer regime in deep wind farms. Phys Rev Fluids 3(12):124603
Calaf M, Meneveau C, Meyers J (2010) Large eddy simulation study of fully developed wind-turbine array boundary layers. Phys Fluids 22(1):015110
Calderer A, Yang X, Angelidis D, Khosronejad A, Le T, Kang S, Gilmanov A, Ge L, Borazjani I (2015) Virtual flow simulator. Univ. of Minnesota, Minneapolis, MN (United States), Tech rep
Cañadillas B, Beckenbauer M, Trujillo JJ, Dörenkämper M, Foreman R, Neumann T, Lampert A (2022) Offshore wind farm cluster wakes as observed by long-range-scanning wind lidar measurements and mesoscale modeling. Wind Energy Sci 7(3):1241–1262
Chamorro LP, Porté-Agel F (2010) Flow characterization of wind-turbine wake (s) developed in a boundary layer flow with different thermal stratifications: a wind-tunnel study. In: The fifth international symposium on computational wind engineering, North Carolina, USA
Chamorro LP, Arndt R, Sotiropoulos F (2011) Turbulent flow properties around a staggered wind farm. Boundary-Layer Meteorol 141(3):349–367
Christiansen MB, Hasager CB (2005) Wake effects of large offshore wind farms identified from satellite SAR. Remote Sens Environ 98(2–3):251–268
Churchfield MJ, Lee S, Michalakes J, Moriarty PJ (2012) A numerical study of the effects of atmospheric and wake turbulence on wind turbine dynamics. J Turbul 13:N14
Dong G, Li Z, Qin J, Yang X (2022) How far the wake of a wind farm can persist for? Theor Appl Mech Lett 12(1):100314
Emeis S (2010) A simple analytical wind park model considering atmospheric stability. Wind Energy 13(5):459–469
Feng D, Li LK, Gupta V, Wan M (2022) Componentwise influence of upstream turbulence on the far-wake dynamics of wind turbines. Renew Energy 200:1081–1091
Gadde SN, Stevens RJ (2021) Interaction between low-level jets and wind farms in a stable atmospheric boundary layer. Phys Rev Fluids 6(1):014603
Ge L, Sotiropoulos F (2007) A numerical method for solving the 3d unsteady incompressible Navier–Stokes equations in curvilinear domains with complex immersed boundaries. J Comput Phys 225(2):1782–1809
Germano M, Piomelli U, Moin P, Cabot WH (1991) A dynamic subgrid-scale eddy viscosity model. Phys Fluids A 3(7):1760–1765
Hasager CB, Vincent P, Badger J, Badger M, Di Bella A, Peña A, Husson R, Volker PJ (2015) Using satellite SAR to characterize the wind flow around offshore wind farms. Energies 8(6):5413–5439
Jimenez A, Crespo A, Migoya E, García J (2007) Advances in large-eddy simulation of a wind turbine wake. J Phys Conf Ser 75:012041
Kadum H, Cal RB, Quigley M, Cortina G, Calaf M (2020) Compounded energy gains in collocated wind plants: energy balance quantification and wake morphology description. Renew Energy 150:868–877
Kim YH, Lim HC (2017) Effect of island topography and surface roughness on the estimation of annual energy production of offshore wind farms. Renew Energy 103:106–114
Lamare ML, Hedley JD, King MD (2023) The effects of surface roughness on the calculated, spectral, conical-conical reflectance factor as an alternative to the bidirectional reflectance distribution function of bare sea ice. Cryosphere 17(2):737–751
Li Z, Liu X, Yang X (2022) Review of turbine parameterization models for large-eddy simulation of wind turbine wakes. Energies 15(18):6533
Lundquist J, DuVivier K, Kaffine D, Tomaszewski J (2019) Costs and consequences of wind turbine wake effects arising from uncoordinated wind energy development. Nat Energy 4(1):26–34
Ma X, Chen Y, Yi W, Wang Z (2021) Prediction of extreme wind speed for offshore wind farms considering parametrization of surface roughness. Energies 14(4):1033
Maas O (2022) From gigawatt to multi-gigawatt wind farms: wake effects, energy budgets and inertial gravity waves investigated by large-eddy simulations. Wind Energy Sci Discuss 1:1–31
Maas O, Raasch S (2022) Wake properties and power output of very large wind farms for different meteorological conditions and turbine spacings: a large-eddy simulation case study for the german bight. Wind Energy Sci 7(2):715–739
McCarty BJ, Churnside JH (2016) Comparing near surface measurements of wind speed and direction over the indian ocean from lidar and scatterometer, and results from predictive study using the wind shear power law and the surface roughness log law to model upper level winds from near surface measurements. The National Oceanic and Atmospheric Administration
Meyers J, Meneveau C (2012) Optimal turbine spacing in fully developed wind farm boundary layers. Wind Energy 15(2):305–317

Ning X, Wan D (2019) Les study of wake meandering in different atmospheric stabilities and its effects on wind turbine aerodynamics. Sustainability 11(24):6939
Platis A, Siedersleben SK, Bange J, Lampert A, Bärfuss K, Hankers R, Cañadillas B, Foreman R, Schulz-Stellenfleth J, Djath B et al (2018) First in situ evidence of wakes in the far field behind offshore wind farms. Sci Rep 8(1):1–10
Platis A, Hundhausen M, Mauz M, Siedersleben S, Lampert A, Bärfuss K, Djath B, Schulz-Stellenfleth J, Canadillas B, Neumann T et al (2021) Evaluation of a simple analytical model for offshore wind farm wake recovery by in situ data and weather research and forecasting simulations. Wind Energy 24(3):212–228
Pope SB (2000) Turbulent flows. Cambridge University Press, Cambridge
Porté-Agel F, Wu YT, Lu H, Conzemius RJ (2011) Large-eddy simulation of atmospheric boundary layer flow through wind turbines and wind farms. J Wind Eng Ind Aerodyn 99(4):154–168
Porté-Agel F, Bastankhah M, Shamsoddin S (2020) Wind-turbine and wind-farm flows: a review. Boundary-Layer Meteorol 174:1–59
Pratt D (1980) Two-dimensional model variability in thermal inertia surveys. Remote Sens Environ 9(4):325–338
Rolin VF, Porté-Agel F (2018) Experimental investigation of vertical-axis wind-turbine wakes in boundary layer flow. Renewable Energy 118:1–13
Siedersleben SK, Lundquist JK, Platis A, Bange J, Bärfuss K, Lampert A, Cañadillas B, Neumann T, Emeis S (2018) Micrometeorological impacts of offshore wind farms as seen in observations and simulations. Environ Res Lett 13(12):124012
Stevens RJ (2016) Dependence of optimal wind turbine spacing on wind farm length. Wind Energy 19(4):651–663
Stevens RJ, Meneveau C (2017) Flow structure and turbulence in wind farms. Annu Rev Fluid Mech 49:311–339
Stevens RJ, Gayme DF, Meneveau C (2016) Effects of turbine spacing on the power output of extended wind-farms. Wind Energy 19(2):359–370
Stieren A, Stevens RJ (2021) Evaluating wind farm wakes in large eddy simulations and engineering models. J Phys: Conf Ser 1934:012018
Stieren A, Stevens RJ (2022) Impact of wind farm wakes on flow structures in and around downstream wind farms. Flow 2:E21
Syed AH, Mann J, Platis A, Bange J (2022) Turbulence structures and entrainment length scales in large offshore wind farms. Wind Energy Sci Discuss 1:1–22
Wu YT, Porté-Agel F (2013) Simulation of turbulent flow inside and above wind farms: model validation and layout effects. Boundary-Layer Meteorol 146(2):181–205
Yang X, Zhang X, Li Z, He GW (2009) A smoothing technique for discrete delta functions with application to immersed boundary method in moving boundary simulations. J Comput Phys 228(20):7821–7836
Yang X, Kang S, Sotiropoulos F (2012) Computational study and modeling of turbine spacing effects in infinite aligned wind farms. Phys Fluids 24(11):115107
Yang X, Angelidis D, Khosronejad A, Le T, Kang S, Gilmanov A, Ge L, Borazjani I, Calderer A (2015a) Virtual flow simulator (Computer Software). https://doi.org/10.11578/dc.20171025.1758
Yang X, Sotiropoulos F, Conzemius RJ, Wachtler JN, Strong MB (2015) Large-eddy simulation of turbulent flow past wind turbines/farms: the virtual wind simulator (VWiS). Wind Energy 18(12):2025–2045
Zhang M, Arendshorst MG, Stevens RJ (2019) Large eddy simulations of the effect of vertical staggering in large wind farms. Wind Energy 22(2):189–204